



1 **Climate changes during the Lateglacial in South Europe: new insights**
2 **based on pollen and brGDGTs of Lake Matese in Italy**

3 Mary Robles^{1,2}, Odile Peyron², Guillemette Ménot³, Elisabetta Brugiapaglia¹, Sabine Wulf⁴, Oona Appelt⁵,
4 Marion Blache², Boris Vannièr^{6,7}, Lucas Dugerdil², Bruno Paura¹, Salomé Ansanay-Alex³, Amy Cromartie⁸,
5 Laurent Charlet⁹, Stephane Guédron⁹, Jacques-Louis de Beaulieu¹⁰, Sébastien Joannin^{2,4}

6
7 ¹ Univ. Molise, Department of Agricultural, Environmental and Food Sciences, Campobasso, Italy
8 ² Univ. Montpellier, CNRS, IRD, EPHE, UMR 5554 ISEM, Montpellier, France
9 ³ Univ. Lyon, ENSL, UCBL, UJM, CNRS, LGL-TPE, F-69007 Lyon, France
10 ⁴ Univ. Portsmouth, School of the Environment, Geography and Geosciences, Portsmouth, United Kingdom
11 ⁵ Helmholtz Centre Potsdam, GFZ German Research Centre of Geosciences, Section 3.6, Telegrafenberg,
12 Potsdam, Germany
13 ⁶ Chrono-Environnement, CNRS, Univ. Bourgogne Franche-Comté, Besançon, France
14 ⁷ MSHE Ledoux, CNRS, Université Bourgogne Franche-Comté, Besançon, France
15 ⁸ Cornell Univ., Department of Anthropology, Ithaca, NY, USA
16 ⁹ Univ. Grenoble Alpes, Univ. Savoie Mont Blanc, CNRS, IRD, IFSTTAR, ISTERre, Grenoble, France
17 ¹⁰ Aix-Marseille Univ., CNRS, IRD, UMR 7263 & 237 IMBE, Aix-en-Provence, France

18
19 E-mails : Mary Robles, mary.robles@umontpellier.fr; Odile Peyron, odile.peyron@umontpellier.fr
20
21

22 **Short Abstract**

23 Quantitative climate reconstructions based on pollen and brGDGTs reveal, for the
24 Lateglacial, a warm Bølling–Allerød and a marked cold Younger Dryas in Italy, showing no
25 latitudinal differences in terms of temperatures across Italy. In terms of precipitation, no
26 latitudinal differences are recorded during the Bølling–Allerød whereas the latitudes 40–42°N
27 appear as a key junction point between wetter conditions in Southern Italy and drier conditions
28 in Northern Italy during the Younger Dryas.

29

30 **Abstract**

31 The Lateglacial (14,700–11,700 cal BP) is a key climate period marked by rapid but
32 contrasted changes in the Northern Hemisphere. Indeed, regional climate differences have been
33 evidenced during the Lateglacial in Europe and the Northern Mediterranean areas. However,
34 past climate patterns are still debated since temperature and precipitation changes are poorly
35 investigated towards the lower European latitudes. Lake Matese in Southern Italy is a key site
36 in the Central Mediterranean to investigate climate patterns during the Lateglacial. This study
37 aims to reconstruct climate changes and their impacts at Matese using a multi-proxy approach
38 including magnetic susceptibility, geochemistry (XRF core scanning), pollen data and
39 molecular biomarkers like branched Glycerol Dialkyl Glycerol Tetraethers (brGDGTs).



40 Palaeotemperatures and -precipitation patterns are quantitatively inferred from pollen
41 assemblages (multi-method approach: Modern Analogue Technique, Weighted Averaging
42 Partial Least Squares regression, Random Forest, and Boosted Regression Trees) and brGDGTs
43 calibrations. The results are compared to a latitudinal selection of regional climate
44 reconstructions in Italy to better understand climate processes in Europe and in the circum-
45 Mediterranean region. A warm Bølling–Allerød and a marked cold Younger Dryas are revealed
46 in all climate reconstructions inferred from various proxies (chironomids, ostracods,
47 speleothems, pollen, brGDGTs), showing no latitudinal differences in terms of temperatures
48 across Italy. During the Bølling–Allerød, no significant changes in terms of precipitation are
49 recorded, however, a contrasted pattern is visible during the Younger Dryas. Slightly wet
50 conditions are recorded south of latitude 42°N whereas dry conditions are recorded north of
51 latitude 42°N. During the Younger Dryas, cold conditions can be attributed to the southward
52 position of North Atlantic sea-ice and of the Polar Frontal JetStream whereas the increase of
53 precipitation in Southern Italy seems to be linked to relocation of Atlantic storm tracks into the
54 Mediterranean, induced by the Fennoscandian ice sheet and the North European Plain. On the
55 contrary, during the Bølling–Allerød warm conditions can be linked to the northward position
56 of North Atlantic sea-ice and of the Polar Frontal JetStream.

57

58 **Keywords: Mediterranean region; Palynology; Molecular Biomarker; Paleoclimate;**
59 **Transfer functions; Tephra; Younger Dryas; Bølling–Allerød; Lateglacial**

60

61 **1. Introduction**

62

63 In the Northern Hemisphere, the Lateglacial (ca. 14,700–11,700 cal BP) is a period of
64 special climatic interest characterized by contrasted and rapid climate changes, associated with
65 the successive steps of the deglaciation and changes in atmospheric and ocean circulation
66 patterns (e.g., Walker et al., 2012; Rehfeld et al., 2018). Following the cold Oldest Dryas (OD)
67 period, the Bølling–Allerød (B/A) or Greenland Interstadial-1 (GI-1) began abruptly at 14,700
68 cal BP with warmer conditions. At 12,900–11,700 cal BP, the Younger Dryas (YD) or Greenland
69 Stadial-1 (GS-1) was the last main millennial-scale cold event in Europe during the Lateglacial
70 (Greenland ice-core records; Rasmussen et al., 2014). The YD is characterized by extreme cold,
71 relative dry and windy climate conditions in northern-central Europe (Hepp et al., 2019).
72 Climate become distinctly warmer at 11,700 cal BP with the onset of the Holocene Interglacial



73 (Rasmussen et al., 2014). These rapid and marked climate oscillations have been observed in
74 the Greenland ice core records (Rasmussen et al., 2014) and in Europe from various proxies
75 such as pollen, oxygen isotopes, molecular biomarkers, beetles, and chironomids (e.g. Coope
76 and Lemdahl, 1995; Ammann et al., 2000; Coope and Lemdahl, 1995; Peyron et al., 2005;
77 Lotter et al., 2012; Millet et al., 2012; Blaga et al., 2013; Moreno et al., 2014; Heiri et al., 2015;
78 Poneel et al., 2022; Duprat-Oualid et al., 2022).

79 Regional climate differences have been evidenced during the Lateglacial, and
80 temperature trends in Europe and the Mediterranean region are still a matter of active research
81 and debate. The chironomid-based synthesis of Heiri et al. (2014) suggests that temperature
82 variations during the Lateglacial tend to be more pronounced in Western Europe (British Isles,
83 Norway) than in Southwestern Europe, Central and Southeastern regions. This is particularly
84 true for the Younger Dryas cooling which is not well evidenced in East and Central Southern
85 Europe (Heiri et al., 2014).

86 Diverging temperature trends are also reconstructed from different proxies during key
87 periods of the Lateglacial. Studies suggest that (1) the OD was cooler than the YD in Southern
88 and Central Europe in comparison with Northern Europe (Heiri et al., 2014; Moreno et al.,
89 2014); (2) the Allerød period was warmer than the Bølling in the Southwestern Europe and
90 Mediterranean area (Moreno et al., 2014); and (3) temperatures were more contrasted during
91 the B/A and YD in the North-West of Europe in comparison to the South of Europe (Renssen
92 and Isarin, 2001; Moreno et al., 2014; Heiri et al., 2014). In contrast to temperature, the
93 precipitation signal is poorly known in Europe during the Lateglacial because few proxies are
94 available to quantitatively reconstruct precipitation change. Climate models (GCMs) simulate
95 significant hydrological changes during the B/A and contrasted North-South patterns during the
96 YD (Renssen and Isarin, 2001; Rea et al., 2020). They simulate drier conditions in Northern
97 Europe and wetter conditions in Southern Europe, i.e. in the South of Italy, the Dinaric Alps,
98 and Northern Turkey (Rea et al., 2020). Climate changes during the YD are attributed to a weak
99 Atlantic Meridional Overturning Circulation (AMOC) and a southward shift of the Polar
100 Frontal JetStream (PFJS), linked to the elevation of the ice sheet, in particular the Laurentide
101 ice sheet (Renssen and Isarin, 2001; Renssen et al., 2015; Rea et al., 2020). Rea et al. (2020)
102 also explains the regional climate patterns in Europe by a relocation of Atlantic storm tracks
103 along the western European margin and into the Mediterranean.

104 The understanding of climate processes in Europe and Mediterranean regions during the
105 Lateglacial still needs to be improved. The majority of climate reconstructions are focused on
106 temperatures, and changes in precipitation remain elusive. The “key” junction area between



107 Northern and Southern Europe and regional climatic patterns also needs to be better defined.
108 Moreover, the proxies used to reconstruct climate changes (e.g., coleoptera, chironomids,
109 pollen, ostracods, speleothems) can show differences in terms of amplitudes or patterns which
110 are not only affected by temperatures, but also by precipitation or effective moisture (Moreno
111 et al., 2014; Samartin et al., 2017). For these reasons, more reliable temperature reconstructions,
112 especially from Western Europe and the Mediterranean region are required to test diverging
113 trends during the Lateglacial. The proxies largely used to quantitatively reconstruct past climate
114 changes are often a single proxy approach (e.g. Heiri et al., 2015; Gandouin et al., 2016; Peyron
115 et al., 2017; Marchegiano et al., 2020; Duprat-Oualid et al., 2022). Multiproxy approaches on
116 the same sedimentary record, including independent climate proxies, are necessary to better
117 understand the climate processes in Europe during the Lateglacial (Lotter et al., 2012; Ponelet
118 et al., 2022). Pollen-based reconstructions have the advantage of reconstructing temperatures,
119 precipitation, and seasonality, however, the climate signal can be perturbed by other factors
120 such as CO₂ changes and human impact influencing vegetation development (Peyron et al.,
121 2005). Over the last decades, novel proxies based on molecular geochemistry have been
122 developed and molecular biomarkers are being increasingly used to reconstruct temperatures
123 and represent a complementary proxy for lake sediments (Castañeda and Schouten, 2011). In
124 particular, branched Glycerol Dialkyl Glycerol Tetraethers (brGDGTs) are ubiquitous organic
125 compounds synthesized by bacteria (Weijers et al., 2006) which have been useful for
126 reconstruction environmental parameters. To date, the actual producers of brGDGTs remain
127 somewhat unknown although it is proposed they come from the phylum *Acidobacteria* (Weijers
128 et al., 2009; Sinninghe Damsté et al., 2018). The relationship, however, between brGDGT
129 distribution and environmental changes, in particular pH and temperature, are well established
130 (Naafs et al., 2017b, 2017a; Dearing Crampton-Flood et al., 2020; Martínez-Sosa et al., 2021;
131 Raberg et al., 2021). The degree of methylation of brGDGTs (MBT; methylation of branched
132 GDGTs) varies depending on the mean annual air temperature (MAAT) and higher fractional
133 abundance of hexa- (III) and penta- (II) methylated brGDGTs are recorded in colder
134 environments (Weijers et al., 2007). Branched glycerol dialkyl glycerol tetraether (brGDGT)
135 membrane lipids are increasingly used as a temperature proxy: in Europe, brGDGTs have been
136 used to reconstruct the Mid to Late Holocene temperature changes in the Carpathians (Ramos-
137 Román et al., 2022), the last 36,000 years in the Southern Iberian Peninsula (Rodrigo-Gámiz et
138 al., 2022), the Holocene temperatures in France (Martin et al., 2020), and in the Eastern
139 Mediterranean over the last deglaciation (Sanchi et al., 2014; Stockhecke et al., 2021). The
140 association in the same core between brGDGTs and other proxies such as pollen for climate



141 reconstructions are still rare (Watson et al., 2018; Martin et al., 2020; Dugerdil et al., 2021a,
142 2021b; Ramos-Román et al., 2022; Robles et al., 2022) and no study are yet available for the
143 circum-Mediterranean region during the Lateglacial.

144 This study presents a high-resolution climate reconstruction for the Lateglacial period in
145 South Central Europe, inferred from multi-proxy data of the Lake Matese sedimentary record
146 (Southern Italy). In detail, the aims of this study are to:

147 1) establish reliable and independent quantitative climate reconstructions based on
148 molecular biomarkers (brGDGTs) and pollen data to help identify potential biases of currently
149 used proxies and thus improve the reliability of each proxy-inferred climate record;

150 2) compare these reconstructions with regional climate reconstructions and in the light of
151 other South European records;

152 3) better understand the climate processes in Europe and Mediterranean during the
153 Lateglacial period.

154

155 2. Study site

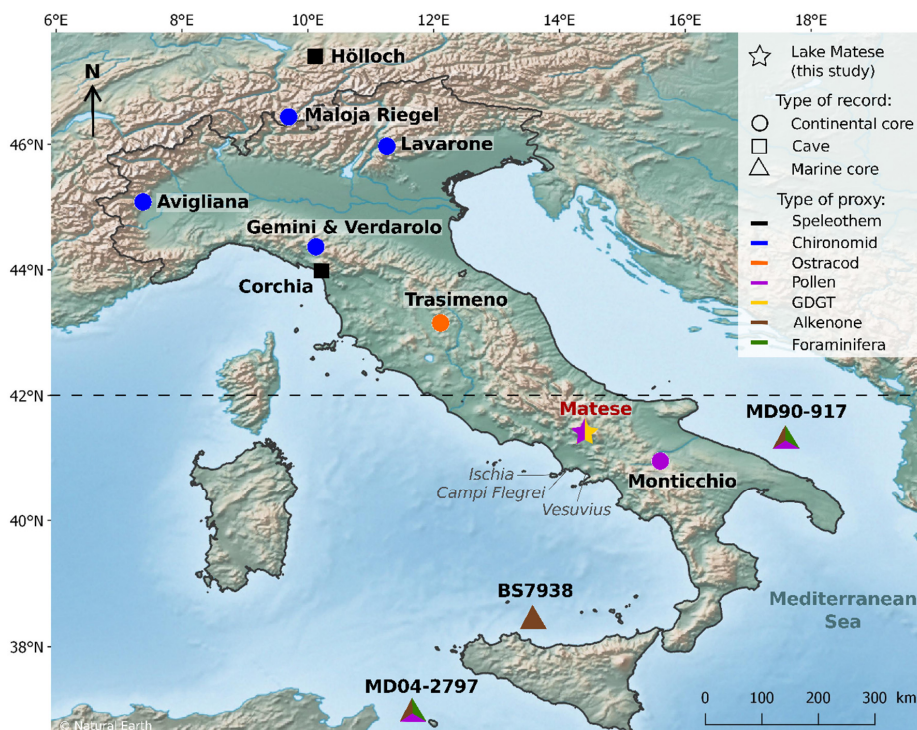
156

157 Lake Matese (41°24'33.3"N, 14°24'22.1"E, 1012 m a.s.l.) is located in the Caserta
158 province in the Campania region, Southern Italy, approximately 60 km north of the city of
159 Naples and the active Campanian volcanoes (Vesuvius, Campi Flegrei, Ischia) (Fig. 1). The
160 lake is situated in the Matese karst massif in the Southern Apennines, which extends over 30
161 km from the NE to the SW and is composed of Late Triassic-Miocene limestones and dolomites
162 (Fiorillo and Doglioni, 2010). The present formation of the massif was the result of an extension
163 by strike-slip faults during the Quaternary, and several strong earthquakes were recorded in the
164 massif (Ferranti et al., 2015; Ferrarini et al., 2017; Galli et al., 2017; Valente et al., 2019). Lake
165 Matese is the highest karst lake of Italy and is surrounded by the two highest peaks of the massif,
166 Mount Miletto (2050 m a.s.l.) and Mount Gallinola (1923 m a.s.l.), which feed the lake by their
167 snowmelt. Along the southern side of the lake, two sinkholes named the “Breccie” and
168 “Scennerato” are present (Fiorillo and Pagnozzi, 2015). In the 1920s, hydraulic works were
169 conducted to isolate the bottom of the lake and the main sinkholes by earthen dams (Fiorillo
170 and Pagnozzi, 2015). The water level of the lake improved from 1007-1009 m a.s.l. to 1012 m
171 a.s.l. with a volume of 15 mm³ (Fiorillo and Pagnozzi, 2015). A part of the lake water is
172 transported to the hydroelectric power station of Piedimonte Matese at the bottom of the
173 mountain massif.



174 The Matese Mountains are characterized by a Mediterranean warm-temperate, humid
175 climate (Aucelli et al., 2013). The southwestern part of the massif, including Lake Matese, have
176 the highest precipitation with a maximum at Campitello Matese (1400 m a.s.l.) (Fiorillo and
177 Pagnozzi, 2015). Lake Matese shows an annual precipitation of 1808 mm with a maximum in
178 November (~290 mm) and December (~260 mm) and a minimum in July (~50 mm) (Fiorillo
179 and Pagnozzi, 2015). The annual temperatures correspond to 9.3°C with a minimum in January
180 (2°C) and a maximum in July (19°C) (Fiorillo and Pagnozzi, 2015). The precipitation is less
181 important in the southeastern part of the massif due to the Atlantic origin of storms and
182 orographic effect of mountains (Fiorillo and Pagnozzi, 2015).

183 The vegetation of the Matese massif is dominated by deciduous *Quercus* and *Ostrya*
184 *carpinifolia*, while the highest altitudes at the northern flank also show an exposure of *Fagus*
185 *sylvatica* and the lower altitudes of the southern flank includes Mediterranean taxa such as
186 *Quercus ilex* (Taffetani et al., 2012; Carranza et al., 2012; Guarino et al., 2015). The
187 hygrophilous vegetation at Lake Matese is distinguished by the presence of woody (e.g. *Salix*
188 *alba*, *S. caprea*, *S. cinerea* subsp. *cinerea*, *Populus nigra*, *P. alba*), helophytes (e.g. *Phragmites*
189 *australis*, *Schoenoplectus lacustris*, *Typha angustifolia*, *T. latifolia*) and hydrophytes species
190 (*Myriophyllum spicatum*, *Persicaria amphibia*).



191

Figure 1. Location of the Lake Matese and Lateglacial paleoclimate records : Höllloch (Li et al., 2021), Maloja Riegel (Heiri et al., 2014), Lago di Lavarone (Heiri et al., 2014), Lago Piccolo di Avigliana (Larocque and Finsinger, 2008), Lago Gemini (Samartin et al., 2017), Lago Verdarolo (Samartin et al., 2017), Corchia cave (Regattieri et al., 2014), Lake Trasimeno (Marchegiano et al., 2020), Lago Grande di Monticchio (Allen et al., 2002), MD90-917 (Combourieu-Nebout et al., 2013; Sicre et al., 2013), BS7938 (Sbaffi et al., 2004), MD04-2797 (Desprat et al., 2013; Sicre et al., 2013). Dotted line indicates latitude 42°N. Location of active Campanian volcanoes (Vesuvius, Campi Flegrei, Ischia).

192

193 3. Material and methods

194

195 3.1 Coring retrieval

196

Coring of Lake Matese was performed in July 2019 in the southwestern part of the lake (41°24'33.3"N, 14°24'22.1"E, 1012 m a.s.l.). Coring occurred on a floating raft composed of *Salix* spp. and *Phragmites* spp., naturally present in the eastern part of the lake. Three parallel cores (cores A, B and C) were taken with a 1 m Russian corer with a chamber diameter of 6.3 cm. The master core, measuring 535 cm, was constructed from sections of parallel cores and is based on the lithology and XRF data.

202



203 3.2 Chronology and age-depth model

204 Several methods have been used to build the chronology of the core including
205 radiocarbon dating, and tephrochronology. The regional pollen stratigraphy is used to validate
206 this age-depth model. Twelve accelerator mass spectrometry (AMS) ^{14}C dates were measured
207 at Poznań Radiocarbon Laboratory and at the Radiocarbon Dating Center in Lyon. Plant
208 macrofossils (plant fibers, wood) and charcoal were selected for four samples, and bulk
209 sediment was used for eight samples according to the sediment type. Radiocarbon ages were
210 calibrated in years cal BP using the *Calib 8.2* software with the IntCal20 calibration curve
211 (Reimer et al., 2020).

212 Visible tephra layers and cryptotephra layers, detected by magnetic susceptibility and
213 XRF core scanning data, were subsampled and processed for geochemical analysis.
214 Cryptotephra was extracted using H_2O_2 and HCl to remove organic matter and carbonates,
215 sieved at 20 and 100 microns, volcanic glass shards were embedded in resin, sectioned and
216 polished for electron probe microanalysis. A JEOL-JXA8230 probe the Helmholtz Centre
217 Potsdam (Germany) was used with a 15kV accelerating voltage, 10 nA beam current, and a 15
218 micron beam size. Analytical count times were 20 seconds for all elements except for K and
219 Na, measured first at 10 s. International glass standards such as the Max Planck Institute (MPI-
220 glasses) ATHO-G, StHs6/80 and GOR-132 (Jochum et al., 2006) and the natural Lipari obsidian
221 (Hunt and Hill, 1996; Kuehn et al., 2011) were measured prior to sample analysis for data
222 quality insurance. Glass geochemical data of Matese tephtras are normalized on an anhydrous,
223 volatile-free basis and compared with published tephra glass datasets (Wulf et al., 2008; Smith
224 et al., 2011; Tomlinson et al., 2012).

225 The age-depth model based on radiocarbon dates and correlated tephra ages was
226 constructed using an interpolated linear curve with the R ‘Clam’ program with 95% confidence
227 intervals (Blaauw, 2010). In order to validate the age depth models, the pollen stratigraphy of
228 the regional sites was compared with pollen data of Matese. The pollen stratigraphy of Pavullo
229 di Frignano (Vescovi et al., 2010), Lakes Accesa (Drescher-Schneider et al., 2007), Albano
230 (Mercuri et al., 2002), Mezzano (Sadori, 2018), Monticchio (Allen et al., 2002), and Trifoglietti
231 (De Beaulieu et al., 2017) were used to identify the OD-B/A, B/A-YD and YD-Holocene
232 transitions. We used the median age for each transition.

233

234 3.3 Magnetic susceptibility and geochemistry

235 Magnetic susceptibility (MS) was measured with a MS2E1 surface scanning sensor
236 from Bartington Instruments on a Geotek Multi-Sensor Core logger based at the Chrono-



237 environment laboratory (UMR CNRS - University of Franche-Comté). An interval of 3 mm or
238 5 mm was applied depending on the type of sediment.

239 Geochemical analyses were performed at high resolution by X-ray Fluorescence (XRF)
240 with an AVAATECH core scanner at the EDYTEM laboratory (University Savoie Mont
241 Blanc). A continuous 5 mm step measurement was applied with a run at 10 kV and 0.1 mA for
242 15 s to detect lightweight elements, such as Al, Si, K, Ca, Ti, Mn, Fe and a second run at 30 kV
243 and 0.15 mA for 20 s to detect Br, Rb, Sr and Zr. The XRF core scanning provides an estimate
244 of the geochemical composition, and the results are semi-quantitative and expressed as peak
245 intensities counts i.e. counts per second (cps).

246

247 3.4 Pollen analyses

248 A total of 56 samples from the Matese core were collected at 4 cm or 6 cm resolution
249 for pollen analysis. For each sample, 1 cm³ of sediment was processed and 3 *Lycopodium* tablets
250 were added to estimate pollen concentration. Samples were treated following the standard
251 procedure (Faegri et al., 1989; Moore et al., 1991) including HCl, KOH, sieving, acetolysis and
252 HF. The pollen counts were analyzed with a Leica DM1000 LED microscope at a standard
253 magnification of 400x. Pollen taxa were identified using photo atlases (Beug, 2004; Reille,
254 1998; Van Geel, 2002) and a modern reference collection (ISEM, University of Montpellier).
255 Each slide was counted with a minimum of 300 terrestrial pollen grains, excluding aquatic
256 plants such as Cyperaceae, aquatic taxa, and fern spores. A simplified pollen diagram was
257 constructed with the R package *Rioja* (Juggins and Juggins, 2020).

258

259 3.5 Pollen-inferred climate reconstruction

260 A multi-method approach was used to reconstruct climate parameters from pollen data
261 with more reliability than reconstructions based on a single climate reconstruction method
262 (Peyron et al., 2013, 2011, 2005; Salonen et al., 2019). We have selected here the Modern
263 Analog Technique (MAT; Guiot, 1990), Weighted Averaging Partial Least Squares regression
264 (WAPLS; ter Braak and van Dam, 1989; ter Braak and Juggins, 1993), and the most recent
265 machine-learning methods : Random Forest (RF; Breiman, 2001; Prasad et al., 2006) and
266 Boosted Regression Trees (BRT; De'ath, 2007; Elith et al., 2008).

267 The MAT is an assemblage approach, based on the measure of the degree of
268 dissimilarity (squared chord distance) between fossil and modern pollen assemblages (Guiot,
269 1990). Fossil pollen assemblages are compared to a set of modern assemblages (modern
270 dataset), each one associated with climate estimates. The closest modern samples are retained



271 and averaged to estimate past climate conditions (annual and seasonal temperature and
272 precipitation). The WAPLS is a non-linear regression technique that models the relationships
273 between the climate parameters and the pollen taxa from a modern pollen dataset, before
274 applying these relationships to fossil pollen assemblages (ter Braak and Juggins, 1993; ter Braak
275 and van Dam, 1989). WAPLS and MAT methods are applied with the R package *Rioja* (Juggins
276 and Juggins, 2020). RF and BRT, based on machine learning, utilizes regression trees
277 developed with ecological data, and has been used recently to reconstruct palaeoclimatic
278 changes (Salonen et al., 2019; Robles et al., 2022). These classification trees are used to
279 partition the data by separating the pollen assemblages based on the relative pollen percentages.
280 RF is based on a large number of regression trees, each tree being estimated from a randomized
281 ensemble of different subsets of the modern pollen dataset by bootstrapping (Breiman, 2001;
282 Prasad et al., 2006). Finally, the RF prediction is applied on the fossil pollen record. BRT is
283 also based on regression trees (De'ath, 2007; Elith et al., 2008); it differs from RF in the
284 definition of the random modern datasets. In RF, each sample gets the same probability of being
285 selected, while in BRT the samples that were insufficiently described in the previous tree get a
286 higher probability of being selected. This approach is called 'boosting' and increases the
287 performance of the model over the elements that are least well predicted (Breiman, 2001; Prasad
288 et al., 2006; De'ath, 2007; Elith et al., 2008). RF is applied with the R package *randomForest*
289 (Liaw and Wiener, 2002) and BRT with the R package *dismo* (Hijmans et al., 2021).

290 The modern pollen dataset ($n = 3373$ sites) used for the calibration of the methods is
291 based on the large Eurasian/Mediterranean dataset compiled by Peyron et al. (2013, 2017) and
292 completed by Dugerdil et al. (2021a) and Robles et al. (2022). In our study, we added pollen
293 data of 92 surface lake sediments from Italy (Finsinger et al., 2007) and 15 moss polsters from
294 the Matese massif (Robles, 2022). Then, a biome constraint (Guiot et al., 1993), based on the
295 pollen-Plant Functional Type method and following the biomization procedure (Peyron et al.,
296 1998; Prentice et al., 1996) was applied to modern and fossil pollen samples. The modern pollen
297 dataset finally selected for the calibration of the different methods contains 1018 samples
298 belonging to 3 biomes depicted in the fossil core: "warm mixed forest" (WAMX), "temperate
299 deciduous" (TEDE) and "cold steppe" (COST). Performance of each method and calibration
300 training was statistically tested (for more details, see Dugerdil et al., 2021a) to determining if
301 modern samples are suitable for quantitative climate reconstructions. The Root Mean Square
302 Error (RMSE) and the R^2 are presented in the Supplementary Table S1. Five climate parameters
303 were reconstructed, mean annual air temperature (MAAT), mean temperature of the warmest
304 month (MTWA), mean temperature of the coldest month (MTCO), mean annual precipitation



305 (PANN), and winter precipitation (P_{winter} = December, January, and February). For each climate
306 parameter, the methods fitting with the higher R^2 and the lower RMSE were selected.
307 Cyperaceae and ferns in the Matese record have been excluded because they are associated with
308 local dynamics.

309

310 3.6 BrGDGT analyses

311 A total of 56 samples from the Matese core (4 cm or 6 cm resolution) were used for
312 GDGT analysis (same as for pollen analysis). The samples were freeze-dried, powdered and
313 subsampled (1 g for clay and 0.4 g for gyttja). Lipids were extracted from the sediment using a
314 microwave oven (MARS 6; CEM) with dichloromethane:methanol (3:1). Then, the internal
315 standard was added (C_{46} GDGT, Huguet et al., 2006). The total lipid extracts were separated
316 into apolar and polar fractions using a silica SPE cartridge with hexane:DCM (1:1) and
317 DCM:MeOH (1:1). The polar fractions containing brGDGTs were analyzed using a High-
318 Performance Liquid Chromatography Mass Spectrometry (HPLC-APCI-MS, Agilent 1200)
319 with detection via selective ion monitoring (SIM) of m/z 1050, 1048, 1046, 1036, 1034, 1032,
320 1022, 1020, and 1018 in the LGL-TPE of ENS Lyon (Hopmans et al., 2016; Davtian et al.,
321 2018). GDGT concentrations were calculated based on the internal standard. The analytic
322 reproducibility was assessed based on a sediment internal standard.

323

324 3.7 GDGTs annual temperature reconstruction

325 The proportion of tetra- (I), penta- (II) and hexa- (III) methylated brGDGTs includes
326 the fractional abundances of the 5-methyl (X), 6-methyl (X') and 7-methyl (X7) brGDGTs
327 (Ding et al., 2016). The CBT and MBT indexes were defined by Weijers et al. (2007) and the
328 MBT'_{5me} , only based on the 5-methyl brGDGTs, by De Jonge et al. (2014). The Mean Annual
329 Air Temperature (MAAT) was reconstructed with global (Sun et al., 2011) and East African
330 (Russell et al., 2018) lacustrine calibrations. The mean temperature of Months Above Freezing
331 (MAF) was reconstructed with a lacustrine calibration based on Bayesian statistics (Martinez-
332 Sosa et al., 2021; <https://github.com/jesstierney/BayMBT>) and a global lacustrine calibrations
333 with revised compound fractional abundances based on methylation and cyclization number
334 and methylation position (Raberg et al., 2021). Synthesis of the formulae for the main brGDGT
335 indices are presented in Table 1. Modern MAAT and MAF of the Lake Matese corresponds to
336 9.3 °C.

337 The analytic reproducibility corresponds to 0.040 for CBT, 0.0167 for MBT, 0.0206 for
338 MBT'_{5me} , 0.8566 °C for MAAT developed by Sun et al. (2011), 0.6672 °C for MAAT



339 developed by Russell et al. (2018), and 0.5403 °C and 1.1258 °C for MAF_{Meth} and MAF_{Full}
 340 developed by Raberg et al. (2021).
 341

Table 1. Synthesis of the formulae for the main brGDGT indices. For acronym explanation of MAF_{Meth} and MAF_{Full}, see Raberg et al. (2021). For more information about the Bayesian statistics see Martínez-Sosa et al., 2021 and references therein.

Indice	Formula	Reference
%tetra	$\frac{Ia + Ib + Ic}{\Sigma brGDGTs}$	Ding et al., 2016
%penta	$\frac{IIa + IIa' + IIa_7 + IIb + IIb' + IIb_7 + IIc + IIc' + IIc_7}{\Sigma brGDGTs}$	Ding et al., 2016
%hexa	$\frac{IIIa + IIIa' + IIIa_7 + IIIb + IIIb' + IIIb_7 + IIIc + IIIc' + IIIc_7}{\Sigma brGDGTs}$	Ding et al., 2016
CBT	$-\log \frac{Ib + IIb}{Ia + IIa}$	Weijers et al., 2007
MBT	$\frac{Ia + Ib + Ic}{\Sigma brGDGTs}$	Weijers et al., 2007
MBT' _{5me}	$\frac{Ia + Ib + Ic}{Ia + Ib + Ic + IIa + IIb + IIc + IIIa}$	De Jonge et al., 2014
MAAT (°C)	$3.949 - 5.593 \times CBT + 38.213 \times MBT$ ($n = 100, R^2 = 0.73, RMSE = 4.27^\circ C$)	Sun et al., 2011
MAAT (°C)	$-1.21 + 32.42 \times MBT'_{5me}$ ($n = 65, R^2 = 0.92, RMSE = 2.44^\circ C$)	Russell et al., 2018
MAF _{Meth} (°C)	$92.9 + 63.84 \times fib_{Meth}^2 - 130.51 \times fib_{Meth}$ $- 28.77 \times fIIa_{Meth}^2 - 72.28 \times fIIb_{Meth}^2$ $- 5.88 \times fIIc_{Meth}^2 + 20.89 \times fIIIa_{Meth}^2$ $- 40.54 \times fIIIa_{Meth} - 80.47 \times fIIIb_{Meth}$ ($n = 182, R^2 = 0.90, RMSE = 2.14^\circ C$)	Raberg et al., 2021
MAF _{Full} (°C)	$-8.06 + 37.52 \times fIa_{Full} - 266.83 \times fib_{Full}^2$ $+ 133.42 \times fib_{Full} + 100.85 \times fIIa'_{Full}^2$ $+ 58.15 \times fIIIa'_{Full}^2 + 12.79 \times fIIIa_{Full}$ ($n = 182, R^2 = 0.91, RMSE = 1.97^\circ C$)	Raberg et al., 2021
MAF (°C)	Equation from the Bayesian model : $MBT'_{5me} = 0.030(\pm 0.001)MAF + 0.075(\pm 0.012)$ ($R^2 = 0.82, RMSE = 2.9^\circ C$)	Martínez-Sosa et al., 2021

342
 343



344 **4. Results**

345

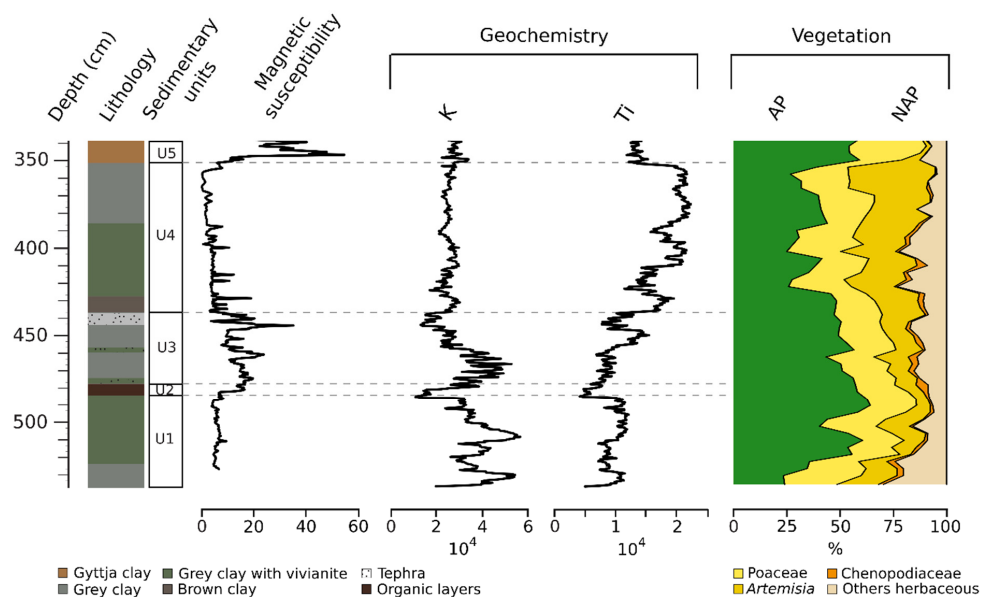
346 4.1 Lithology, magnetic susceptibility, geochemistry and pollen

347 The lithology of Matese core (Fig. 2) is mainly composed of gray clay sediment with
348 vivianite from the base to 350 cm, interrupted by an organic layer between 477-484 cm
349 (sedimentary Unit 2) and a macroscopic visible tephra layer (Fig. 2) between 476-437 cm
350 (sedimentary Unit 3). This part contains few plant fibers, which are essentially vertically
351 oriented in the core. From 349 to 320 cm, the lithology is formed by a mix of clay sediment and
352 gyttja (sedimentary Unit 5). This part is mostly composed by roots and fine rootlets.

353 Magnetic susceptibility (MS) and Potassium (K) peaks of XRF core scanning are used
354 to detect tephra layers (Fig. 2). MS and Potassium contents show increased values at 516-502
355 cm, 482-437 cm and 366-338 cm, which correspond to the deposition of tephra material
356 (macroscopic visible tephra and cryptotephra of primary and secondary deposition). Small
357 peaks are also visible in MS between 430 and 360 cm but they are not associated with any
358 observed tephra. Potassium content is also marked by an increase between 536-526 cm which
359 corresponds to tephra of primary deposition. Titanium (Ti) content, on the other hand, is
360 representative for terrigenous input which is prevailing in sedimentary Unit 4 (Fig. 2).

361 The main pollen taxa diagram (Fig. 2) shows the dominance of herbaceous taxa
362 (Poaceae, *Artemisia*) and a small proportion of arboreal taxa at the base of the sequence. From
363 520 to 425 cm, the period is marked by three expansion phases of arboreal taxa, followed
364 between 438 to 354 cm by a large increase of *Artemisia* and a drop of AP taxa starting at 422
365 cm. Finally, from 354 to 338 cm AP and Poaceae increase, whereas *Artemisia* significantly
366 decline.

367



368

Figure 2. Sediment lithology, magnetic susceptibility, geochemical data and selected terrestrial pollen taxa of Matese. Arboreal Pollen (AP; green) and Non Arboreal Pollen (NAP; yellow-orange) are expressed in percentages of total terrestrial pollen.

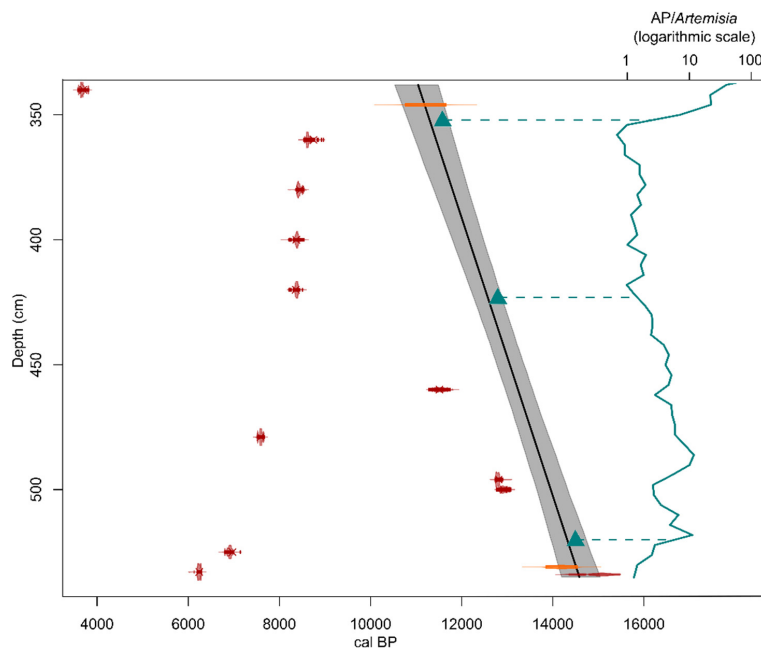
369 4.2 Age-depth model

370 The age-depth model is based on ^{14}C dates and tephrochronology, and then pollen
371 stratigraphy was used to validate the age-depth model (Fig. 3). Based on their typical phono-
372 trachytic and bimodal tephri-phonolitic to trachytic major element glass composition Matese
373 tephtras at 530 cm and 346 cm depth can be correlated with distal Monticchio tephtras TM-8 and
374 TM-6-2, respectively (Fig. 4; Table 2). Tephra TM-8 has been correlated with the Neapolitan
375 Yellow Tuff (NYT) eruption (Wulf et al., 2004) which has an age of $14,194 \pm 172$ cal BP (Bronk
376 Ramsey et al., 2015). The tephra layer at 530 cm corresponds to the primary deposition and
377 secondary deposition of remobilised tephtras that were identified at 510 cm and 475 cm. TM-6-
378 2 most likely are derived from the Early Holocene Casale eruption from Campi Flegrei (Smith
379 et al., 2011) which is varve dated in Monticchio at $11,210 \pm 224$ cal BP (Wulf et al., 2008). The
380 tephra layer at 346 cm corresponds to a primary deposition.

381 The ages obtained with the regional pollen stratigraphy show an OD-B/A transition at
382 $14,500 \pm 93.7$ cal BP, a B/A-YD transition at $12,800 \pm 57.7$ cal BP and a YD-Holocene
383 transition at $11,575 \pm 103.1$ cal BP (Allen et al., 2002; Mercuri et al., 2002; Drescher-Schneider
384 et al., 2007; Vescovi et al., 2010; De Beaulieu et al., 2017; Sadori, 2018). Pollen stratigraphy of



385 the regional sites were compared with pollen data of Matese and the ages obtained show a good
 386 correspondence with the ages of tephra samples but a poor correspondence with the ^{14}C dates.
 387 Therefore, most of the ^{14}C dates (Table 3) are not included in the age-depth model (except the
 388 date at the base of the core).



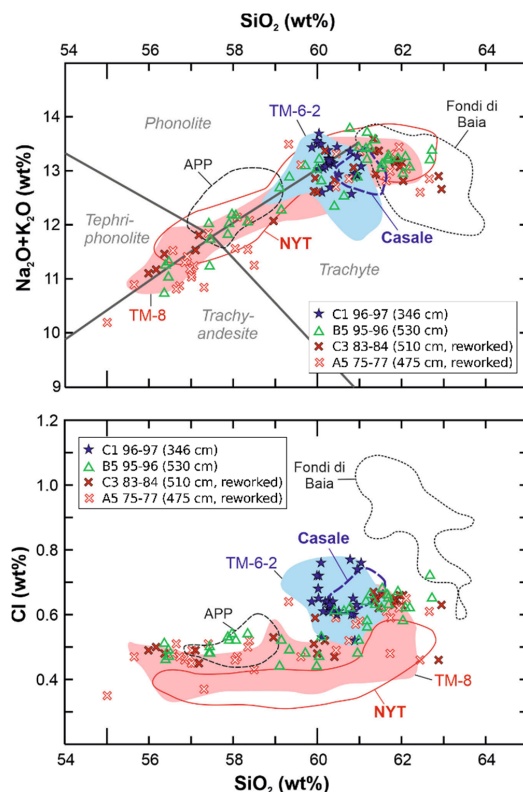
389

Figure 3. Age-depth model is based on calibrated AMS radiocarbon dates (red points; Table 3) and tephra ages (orange points; Table 2). Gray bands are 95% confidence intervals of the age–depth model. Blue triangles are the median of ages of the vegetation transition compiled with the regional pollen stratigraphy. This pollen stratigraphy includes the sites of Pavullo di Frignano (Vescovi et al., 2010), Accessa (Drescher-Schneider et al., 2007), Albano (Mercuri et al., 2002), Mezzano (Sadori, 2018), Monticchio (Allen et al., 2002), and Trifoglietti (De Beaulieu et al., 2017). AP/Artemisia ratio (blue line) is expressed on a logarithmic scale. AP: Arboreal Pollen.

Table 2. Tephra samples from Matese cores (MC) and correlation with tephra samples from Lago Grande di Monticchio (Wulf et al., 2008) and proximal eruptive sources.

Sample ID	Depth MC (cm)	Tephra Monticchio	Eruption	Age (cal BP)	Age reference
C1 96-97	346	TM-6-2	Casale	11,210 ± 224	Wulf et al., 2008
A5 75-77	475 (reworked)	TM-8	Neapolitan Yellow Tuff (NYT)	14,194 ± 172	Bronk Ramsey et al., 2015
C3 83-84	510 (reworked)				
B5 95-96	530				

390



391

Figure 4. Bivariate plot of selected major elements (SiO_2 vs. total alkalis and SiO_2 vs. Cl) of Matese tephtras and potential proximal and Monticchio tephtra correlatives. Data from: TM-6-2 (Monticchio, Wulf et al., 2008; this study); TM-8 (Monticchio, Tomlinson et al., 2012; this study); Casale, Fondi di Baia (proximal; Smith et al., 2011); APP/Agnano Pomici Principali and NYT/Neapolitan Yellow Tuff (proximal; Tomlinson et al., 2012).

Table 3. AMS-radiocarbon dates (Radiocarbon Laboratory, Poznań), calibrated median ages, with 2σ range of calibration from Matese cores (MC).

Sample ID	Depth MC (cm)	Lab code	Material	AMS ^{14}C age (BP)	Age (cal BP) (2σ)	Median age (cal BP)
A4 40-41	340	Poz-128971	Bulk	3425 ± 30	3573 - 3822	3668
A4 60-61	360	Poz-138111	Bulk	7850 ± 40	8540 - 8968	8631
A4 80-81	380	Poz-138112	Bulk	7640 ± 50	8370 - 8541	8432
B4 50-51	400	Poz-128972	Bulk	7580 ± 60	8206 - 8519	8385
A5 20-21	420	Poz-138113	Bulk	7570 ± 50	8206 - 8512	8379
A5 60-61	460	Poz-128976	Bulk	10020 ± 50	11280 - 11743	11519
A6 52-53	479	Poz-119283	Plant fibers, wood fragments, charcoals	6730 ± 40	7513 - 7669	7596
A5 96-97	496	Poz-137155	Wood fragments	10870 ± 60	12728 - 12903	12799
B5 64-65	500	Poz-128973	Bulk	11000 ± 60	12769 - 13078	12925
A6 98-99	525	Poz-119284	Plant fibers	6060 ± 35	6795 - 7147	6912
B5 97-98	533	60747	Plant fibers	5430 ± 30	6190 - 6295	6236
B5 98-99	534	Poz-128975	Bulk	12650 ± 130	14331 - 15477	15027



392

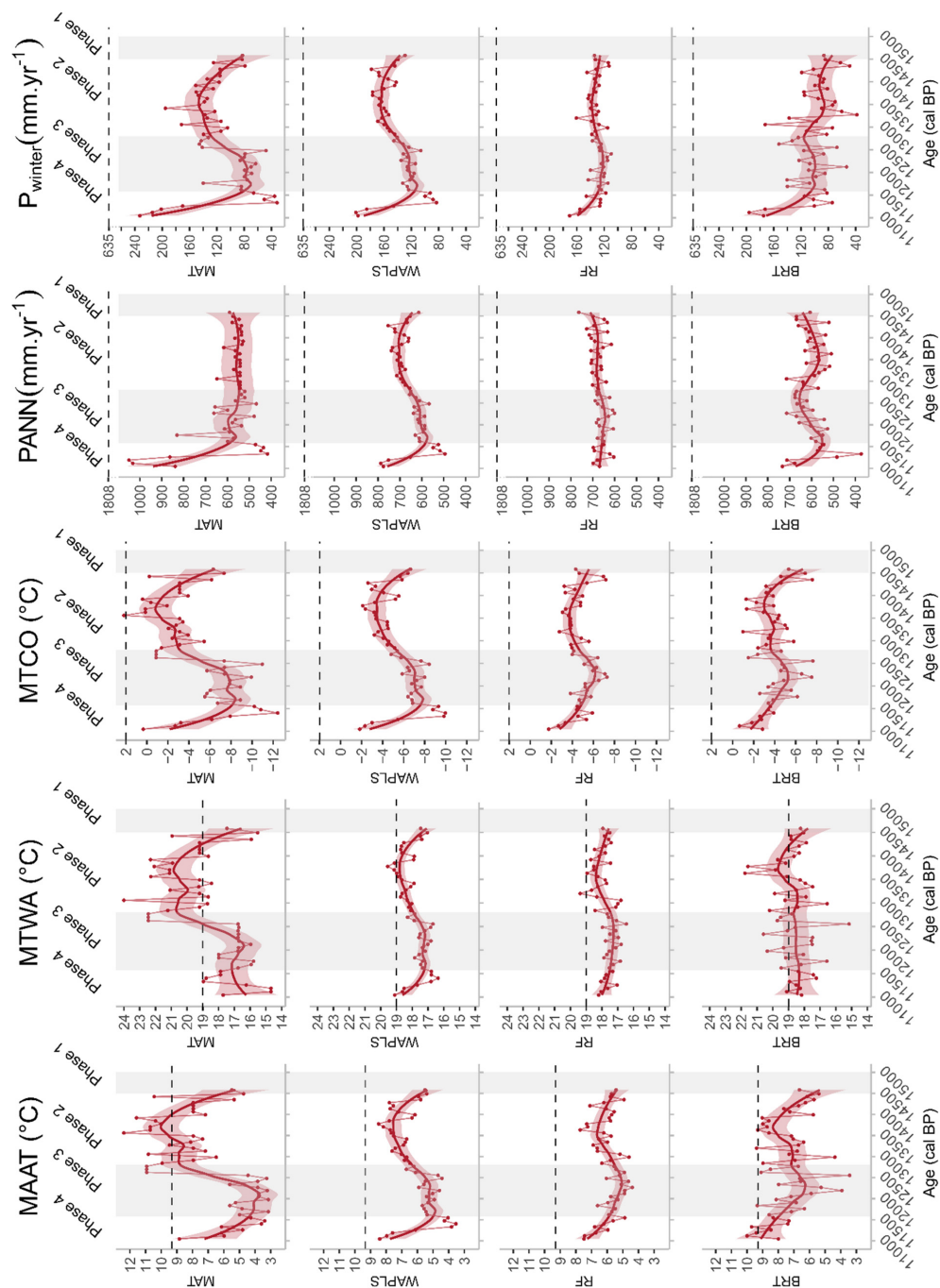
393 4.3 Pollen-inferred climate reconstructions

394 Pollen-inferred climate reconstructions at Matese show similar trends for all methods
395 (Fig. 5). The MAT and the BRT methods show higher sample-to-sample variability than the
396 WAPLS, and RF appears as the less sensitive method. Statistical results of the model
397 performance (Supplementary Table S1) show the better values for R^2 and RMSE for the BRT
398 method (all climatic parameters).

399 Temperature trends show two cold periods (phases 1 and 3) and two warm periods
400 (phases 2 and 4). The reconstructed values (MAAT and MTWA) during the warm periods are
401 close to modern values whereas the values of MTCO are lower than the modern values. Annual
402 precipitation (PANN) shows few variations and the values of PANN and P_{winter} are lower than
403 modern values, with all methods. Phase 1 (535-530 cm; 14,600-14,500 cal BP) is characterized
404 by cold conditions and low precipitation during winter. Phase 2 (530-436 cm; 14,500-12,800
405 cal BP) is a warm period characterized by strong warming and punctuated by three colder events
406 at 14,000 cal BP, 13,500-13,350 cal BP and 13,000 cal BP. Mean annual precipitation shows
407 little variation whereas P_{winter} shows higher values than during the phase 1. Phase 3 (436-367
408 cm; 12,800-11,570 cal BP) is a strong event marked by cold conditions, a slight decline in P_{winter}
409 and few changes for PANN. At the transition with phase 4, a significant decrease in the
410 precipitation parameters is recorded. Phase 4 (367-338 cm; 11,570-11,000 cal BP) is
411 characterized by a well-marked temperature increase (MAAT and MTCO) associated with wet
412 conditions (hydrological parameters reach their maximum value).



413
414



415



416 **Figure 5.** Lake Matese pollen-inferred climate reconstruction based on four methods against age: MAT
417 (Modern Analogue Technique), WAPLS (Weighted Averaging Partial Least Squares regression), RF
418 (Random Forest) and BRT (Boosted Regression Trees). Large lines correspond to loess smoothed
419 curves, shaded areas to the 95% confidence interval and dotted lines to modern climate values of Lake
420 Matese. MAAT: mean annual air temperature. MTWA: mean temperature of the warmest month.
421 MTCO: mean temperature of the coldest month. PANN: mean annual precipitation. P_{winter} : winter
422 precipitation.

423

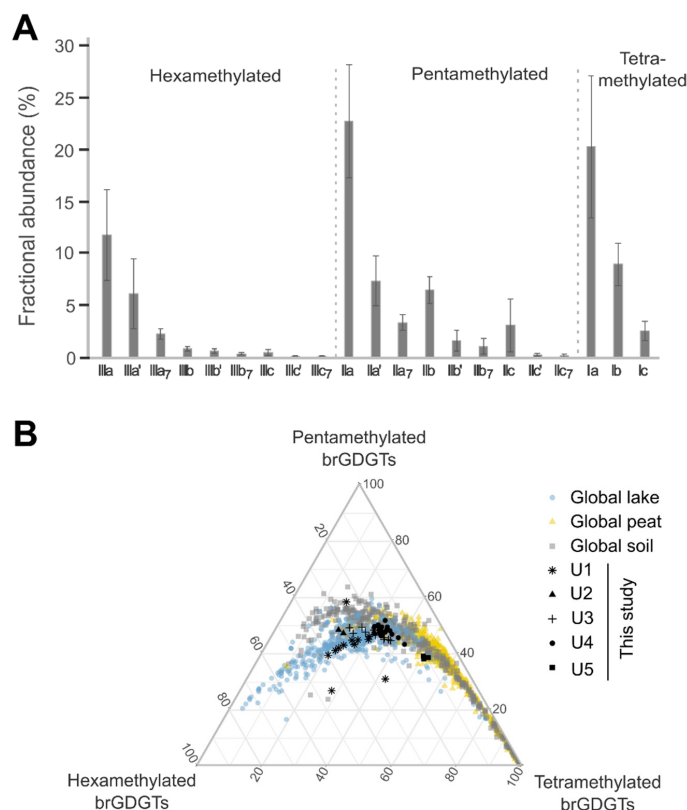
424 4.3 BrGDGT-inferred climate reconstruction

425

426 *4.3.1 Concentration and distribution of brGDGTs*

427 The total concentration of brGDGTs ranges between 0.06 and 8.63 $\mu\text{g}\cdot\text{g}^{-1}$ dry sediment.
428 The fractional abundances of brGDGTs (Fig. 6A) show a dominance of pentamethylated
429 brGDGTs (II, 46%), especially brGDGT IIa (23%), brGDGTs IIa' (7%) and brGDGTs IIb
430 (6%). The relative abundance of tetramethylated brGDGTs (I, 33%) is mainly explained by
431 brGDGT Ia (20%) and brGDGTs Ib (9%). The relative abundance of hexamethylated brGDGTs
432 (III, 21%) is mainly explained by brGDGT IIIa (11%) and brGDGTs IIIa' (6%). The relative
433 abundances of tetra, penta- and hexamethylated brGDGTs of Matese core are compared to
434 global datasets (Fig. 6B). Sediment samples of the Matese core show a good correspondence
435 with global lake and soil samples, except for some samples from sedimentary Unit 1 and 5.
436 Samples of sedimentary Unit 5, characterized by a mix of clay and gyttja, are more similar to
437 global soil and peat samples.

438



439

Figure 6. A) Fractional abundance of tetra-, penta-, and hexamethylated brGDGTs for Matese core. B) Ternary diagram showing the fractional abundances of the tetra-, penta-, and hexamethylated brGDGTs for Matese core (black points) and global lake (blue points; Martínez-Sosa et al., 2021), peat (yellow circles; Naafs et al., 2017a), and soils (gray circles; Yang et al., 2014; Naafs et al., 2017b).

440

441 4.3.2 Indices of brGDGTs

442 The relative abundance of tetra-, penta-, and hexamethylated brGDGTs changes along
 443 Matese core (Fig. 7). The fractional abundance shows a dominance of pentamethylated
 444 brGDGTs except at 518 cm depth, and during the last phase (Phase 4). The fractional abundance
 445 of hexamethylated brGDGTs shows higher values between 535-502 cm and 490-466 cm and
 446 becomes dominant at 486 cm. The fractional abundance of tetramethylated brGDGTs shows
 447 higher values between 502-490 cm and 466-352 cm and is dominant at 518 cm and 352-338
 448 cm (Phase 4).

449 The degree of methylation (MBT, MBT'_{5Me}) and the cyclisation ratio (CBT) also shows
 450 variation along Matese core (Fig. 7). The MBT and the MBT'_{5Me} show similar trends but
 451 different absolute values; they vary between 0.17 and 0.52 and between 0.20 and 0.63,



452 respectively. The degree of methylation remains relatively stable except during two phases of
453 decrease between 534-522 cm and 486-458 cm, and two phases with higher values at 518 cm
454 depth and during the Phase 4. The CBT varies between 0.27 and 0.74. Phase 1 (535-530 cm) is
455 characterized by high values of CBT following by a decline until reaching a minimum between
456 494-482 cm. Then, the CBT slightly increases; at 382 cm a slow decline is recorded, and a
457 strong increase marks Phase 4.

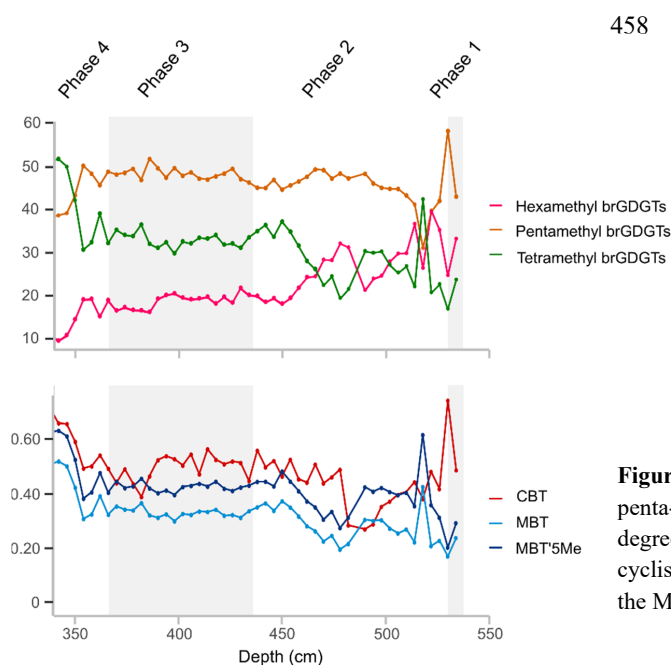


Figure 7. Fractional abundance of tetra-, penta-, and hexamethylated brGDGTs degree of methylation (MBT, MBT'_{5Me}), cyclisation ratio (CBT) against depth for the Matese core.

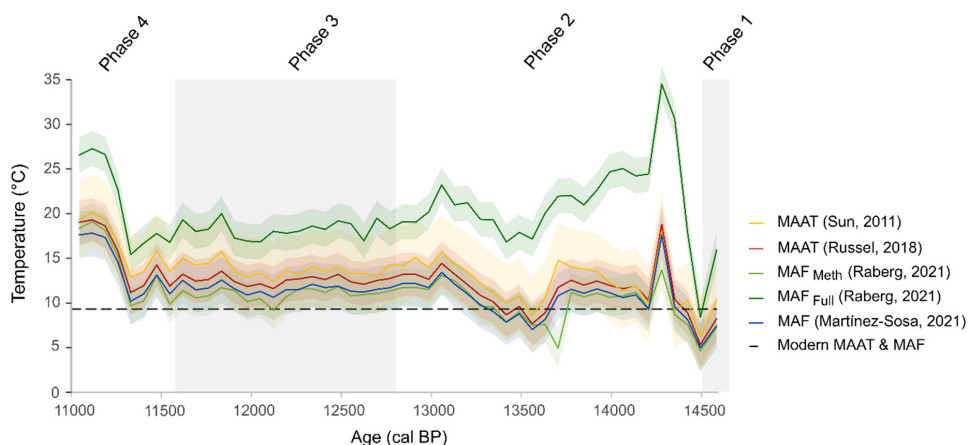
476 *4.3.3 Temperature reconstructions based on brGDGTs*

477 The brGDGT inferred reconstructed MAAT using global (Sun et al., 2011) and East
478 African (Russell et al., 2018) lacustrine calibrations show similar trends than MAF
479 reconstructed using a Bayesian statistical model (Martínez-Sosa et al., 2021) and global (Raberg
480 et al., 2021) lacustrine calibrations (Fig. 8). The values are higher than modern values,
481 especially the values for the MAF_{Full} (Raberg et al., 2021). During Phase 1 (535-530 cm;
482 14,600-14,500 cal BP), all calibrations show cold temperatures. Phase 2 (530-436 cm; 14,500-
483 12,800 cal BP) is marked by an abrupt temperature increase or a stabilization for MAF_{Meth} or a
484 decline for MAF_{Full}. Between 13,700 and 13,200 cal BP, lower temperatures are recorded with
485 all calibrations and from 13,100 cal BP, temperatures slowly decrease until 11,300 cal BP
486 although a slight increase is recorded between 11,900-11,500 cal BP. Phase 4 (367-338 cm;
487 11,570-11,000 cal BP) is characterized by a significant increase of temperature.



488

489



490

Figure 8. Mean Annual Air Temperature (MAAT) based on global (Sun et al., 2011) and East African (Russell et al., 2018) lacustrine calibrations and Mean temperature of Months Above Freezing (MAF) based on Bayesian statistics (Martínez-Sosa et al., 2021) and global (Raberg et al., 2021) lacustrine calibrations against age for the Matese core. Shaded areas correspond to the error associated with calibrations and dotted lines correspond to modern climate values of Lake Matese.

491 5. Discussion

492

493 5.1 Validation of age-depth model

494 The compilation of ages derived from the Italian pollen stratigraphy into the Matese
495 age-model is based on the main vegetation changes identified in the area during the Lateglacial.
496 In summary, the OD in Italian pollen records (and in the present study, Fig. 4) is characterized
497 by an open vegetation dominated by Poaceae, *Artemisia*, with a few arboreal pollen such as
498 *Pinus* and *Juniperus* appearing (Allen et al., 2002; Vescovi et al., 2010; Drescher-Schneider et
499 al., 2007; De Beaulieu et al., 2017; Sadori, 2018). During the B/A, a significant increase of
500 arboreal pollen taxa, including deciduous *Quercus* deciduous, is recorded, and in the majority
501 of records *Betula* appears (Allen et al., 2002; Drescher-Schneider et al., 2007; Vescovi et al.,
502 2010; Sadori, 2018; this study). During the YD, an increase of Poaceae and *Artemisia* (Allen et
503 al., 2002; Mercuri et al., 2002; Drescher-Schneider et al., 2007; Vescovi et al., 2010) and an
504 overall decrease of arboreal pollen taxa, except in Southern Italy, (Allen et al., 2002; Beaulieu
505 et al., 2017; this study) are documented.

506 The ages of tephra samples and ages constrained from the pollen stratigraphy are in
507 good agreement, contrasting results from the ^{14}C dates which are randomly scattered and



508 systematically too young (Fig. 2). The sediments of the Matese core are mainly composed of
509 clay with only few plant fibers. Considering the recurrence of radiocarbon dates between 7570
510 and 7850 cal BP in the core interval between 420 and 360 cm depth (see Table 1), it is
511 hypothesized that the dated organic matter may have originated from penetrating roots of plants
512 growing during sedimentary Unit 5's deposition (Fig. 4). Indeed, aquatic plants of sedimentary
513 Unit 5, identified with pollen, evidence a shallow water body and the development of tree
514 species that typically grow in wetland.

515 Therefore, the overall age-depth model of the Matese core is based on imported, well-
516 accepted tephra ages and one ^{14}C date of a bulk sediment sample from the bottom of the core
517 at 534 cm (Fig. 2).

518

519 5.2 Influence of proxies and methods on climate reconstructions

520

521 *5.2.1 Lake Matese climate signal reliability*

522 Climate reconstructions are based both on pollen and brGDGTs, and some temperature
523 discrepancies (absolute values or amplitudes) are depicted depending on the proxies (Fig. 9).
524 The temperature amplitudes and absolute values are higher for brGDGTs (5-20°C) than the
525 pollen (4-10°C) reconstructions. Pollen-inferred temperature values depend heavily on the
526 quality of the modern pollen dataset including the number of samples, the diversity of samples
527 in terms of biomes, and the similarity with the fossil samples (Chevalier et al., 2020). In our
528 study, the modern database includes several modern samples from the Matese massif, and 95
529 samples from Italy were added to complete the dataset. Moreover, the spatial autocorrelation is
530 low for MAT (Moran's $I < 0.34$, $p\text{-value} < 0.01$), and climate trends are consistent between
531 methods. Reconstructed values for temperatures are close to modern values during the warmest
532 periods, however, precipitation is largely underestimated by all methods for the recent time
533 period (Fig. 5). The same observation was made in Calabria in Southern Italy (Trifoglietti;
534 Joannin et al., 2012), a region also characterized by precipitation above 1700 mm. The
535 underestimation of precipitation is certainly linked to the lack of modern samples located in
536 very wet Mediterranean areas. Considering the brGDGT climate signal, the reconstructed
537 temperatures are overestimated in comparison with modern values (Fig. 8). For shallow
538 temperate lakes (< 20 m), like Lake Matese, our brGDGT reconstructions suggest values
539 anomalously higher than the expected temperature due to thermal variability (seasonal and
540 diurnal; Martínez-Sosa et al., 2021). Lake Matese is located at an altitude of 1012 m a.s.l. and
541 the strong seasonal variability may have influenced the brGDGT distribution. Moreover, the



542 Lake Matese climate reconstructions are based on several global lacustrine calibration datasets,
543 which may not be well adapted to reconstruct paleotemperatures in the Mediterranean region.
544 According to Dugerdil et al. (2021a), local calibrations perform better to reconstruct more
545 reliable absolute values. Unfortunately, at date, only a few global lacustrine calibrations are
546 available, and a local calibration dataset for the Mediterranean region is still missing.

547

548 *5.2.2 Regional climate signal reliability depending on the proxy*

549 Climate reconstructions inferred from Lake Matese are compared to key terrestrial and
550 marine temperature and precipitation records (Fig. 9, 10) in a latitudinal transect in central
551 Mediterranean. These reconstructions for the Mediterranean region are based on different
552 proxies. Most of those are indicators of annual temperatures, but some of them are indicators
553 of seasonal temperature changes. For example, transfer functions based on chironomid
554 assemblages provide estimates of mean July air temperatures (Larocque and Finsinger, 2008;
555 Heiri et al., 2014; Samartin et al., 2017), while ostracod assemblages allow quantitative
556 reconstruction of both January and July palaeotemperatures (Marchegiano et al., 2020).
557 Planktonic foraminifera provide estimates of spring and autumn sea surface temperatures (SST)
558 (Sicre et al., 2013). Molecular biomarkers are considered as indicators of annual temperatures
559 like brGDGTs (this study) or alkenones (Sbaffi et al., 2004; Sicre et al., 2013). For precipitation
560 (Fig. 10), fewer reconstructions are available and they are mainly based on records of pollen
561 (Combourieu-Nebout et al., 2013), $\delta^{18}\text{O}$ *G. bulloides* in marine sediments (Sicre et al., 2013),
562 and $\delta^{18}\text{O}$ in speleothems (Regattieri et al., 2014). Pollen enable the reconstruction of both
563 annual and seasonal temperatures and precipitation (e.g. Allen et al., 2002; Tarroso et al., 2016).

564 The comparison between climate reconstructions inferred from different proxies allows
565 us to identify reliable regional climate signals and to reduce the bias linked to each proxy.
566 Indeed, differences may appear for the timing or amplitudes of changes according to the type
567 of proxy. These differences may be amplified by the proxy provenance, either marine or
568 continental. In Figure 9, the temperature reconstructions above 42°N are mainly based on
569 chironomids, and the climate signal reconstructed is consistent between the sites. In South Italy,
570 at Monticchio, climate reconstructions are based on three pollen records from the same site and
571 differences in terms of amplitude and trend are clearly evidenced (Fig. 9I). These differences
572 are linked to the differences in the core location in the lake and the pollen sample resolution
573 (Allen et al., 2002). The closer the core to the center of the lake (dark blue, Fig. 9I), the better
574 the regional vegetation record and therewith a possible regional climate signal (Peyron et al.,
575 2005). Between latitude 41°N and 36°N, sea-surface temperatures (SSTs) were reconstructed



576 from foraminifera and/or alkenones analyzed from marine cores (Sbaffi et al., 2004; Sicre et
577 al., 2013). Alkenone-based SSTs show a low amplitude of 2-3°C between the B/A and the YD
578 periods, whereas foraminifera-based reconstruction of seasonal temperature show differences
579 of 5-10°C between the B/A and the YD. The differences are linked to their respective methods:
580 For alkenones, the estimation of SSTs are based on the molecular biomarker as the C₃₇ alkenone
581 unsaturation ($U_{37}^{K'}$), whereas, for foraminifera, they are calculated with the MAT method and
582 depend on the occurrence of modern analogues (Sicre et al., 2013).

583

584 5.3 Climate changes during the Lateglacial in Italy

585

586 *5.3.1 Bolling–Allerød warming*

587 The age of transition between the OD and the Bolling–Allerød Interstadial is estimated
588 at around 14,700 cal BP based on the NGRIP ice-core chronology (Rasmussen et al., 2014). In
589 Italy, an abrupt warming is evidenced at ca 14,700 cal BP (Fig. 9). The differences between the
590 different reconstructions seem related to the type of proxy used rather than latitude. The
591 transition is not obvious in the temperature reconstructions based on alkenones (Fig. 9MO;
592 Sbaffi et al., 2004; Sicre et al., 2013), whereas it is well marked in reconstructions based on
593 foraminifera (Fig. 9N; Sicre et al., 2013) and pollen assemblages (Desprat et al., 2013) from
594 the same cores. According to Sicre et al. (2013), alkenones-inferred SSTs could be biased
595 during the Early deglaciation due to water stratification inducing warming of the thin surface
596 water layers where small size nanophytoplankton grow. Except for temperature reconstructions
597 based on alkenones, all the records show an increase of the temperature at the transition OD-
598 B/A (Larocque and Finsinger, 2008; Sicre et al., 2013; Heiri et al., 2014; Marchegiano et al.,
599 2020). The transition, although marked, seems more progressive in the Italian records than in
600 Greenland ice-core but the low resolution of some records can favor this trend. In terms of
601 precipitation (Fig. 10), few records are available in Italy but no significant changes are recorded
602 around 14,700 cal BP by $\delta^{18}\text{O}$ *G. bulloides* (Sicre et al., 2013) and pollen transfer functions
603 (Desprat et al., 2013; this study).

604 The Bolling–Allerød interstadial is a warm interstadial period interrupted by several
605 cold climate oscillations (Rasmussen et al., 2014). According to the synthesis by Moreno et al.
606 (2014), the Bolling was cooler than the Allerød in the Southern Mediterranean compared to the
607 warmer Northern Mediterranean. In Italy, above 42°N, temperature trends are complex to
608 interpret: some records show an increase of temperature (Fig. 9B; Heiri et al., 2014) whereas
609 other records show a decline (Fig. 9CE; Larocque and Finsinger, 2008; Marchegiano et al.,



610 2020). At Matese, pollen and brGDGTs inferred temperatures decrease (Fig. 9F-H), whereas in
611 the southern part of Italy, there are no significant changes during the B/A (Fig. 9I-O; Allen et
612 al., 2002; Saffi et al., 2004; Sicre et al., 2013). Temperature reconstructions in Italy show no
613 distinct difference between the Bølling and the Allerød with respect to the latitude. In terms of
614 amplitude, several studies (Renssen and Isarin, 2001; Heiri et al., 2014; Moreno et al., 2014)
615 suggests that there were less contrasts in temperatures during the B/A in Southern Europe in
616 comparison with Northern Europe. Once again, this difference is not clear in Italy (Fig. 9). At
617 Matese, a significant decrease of brGDGTs-inferred temperature is recorded at 13,700-13,200
618 cal BP (Fig. 9H). This change could be attributed to a colder period such as the Older
619 Dryas or the Inter-Allerød cold period, two short periods characterized by colder conditions in
620 the Greenland ice-core records at 14,000 and 13,100 cal BP, respectively (Rasmussen et al.,
621 2014). However, this cooling event do not appear at the same time in the Matese climate curve
622 based on pollen, and it is only vaguely recorded in other Italian records (Fig. 9). We suggest
623 that this change could be attributed to changes of local conditions that are visible in a lithology
624 change (sedimentary Unit 2, Fig. 4). Indeed, brGDGT distribution and origin can differ
625 according to the type of wetland, water level or vegetation changes (Martínez-Sosa et al., 2021;
626 Robles et al., 2022). In terms of precipitation (Fig. 10), no significant changes occur during the
627 B/A in Italy as suggested previously by Renssen and Isarin (2001) for Southern Europe. The
628 Alpine region seems instead to record wetter conditions during the B/A (Barton et al., 2018; Li
629 et al., 2021).

630

631 5.3.2 A marked Younger Dryas cold event throughout Italy

632 The onset of the YD is estimated around 12,900 cal BP according to the Greenland ice-
633 core chronology (Rasmussen et al., 2014). In Italy, above 42°N, the transition between the B/A
634 and the YD is progressive in terms of temperatures except for chironomid records (Fig. 9B;
635 Heiri et al., 2014). At Matese, pollen-based reconstructions show a progressive decline of
636 temperatures with all methods except the MAT (Fig. 9FG). For this method, the transition is
637 more abrupt, but this difference can be attributed to the application of the biome constraint.
638 BrGDGT-based reconstructions record a steady decrease during the YD or no significant
639 changes according to the calibrations used (Fig. 9H). For southern Italian records, the transition
640 is more abrupt and particularly marked in the foraminifera record in contrast to alkenones-based
641 reconstructions (Fig. 9J-O; Saffi et al., 2004; Sicre et al., 2013). In terms of precipitation (Fig.
642 10), the northern Italian speleothems records show an abrupt transition (Regattieri et al., 2014;



643 Li et al., 2021) whereas the southern Italian pollen and isotopes records do not reveal significant
644 changes (Sicre et al., 2013; Combourieu-Nebout et al., 2013; Desprat et al., 2013).

645 The YD is characterized by cold conditions in the Northern Hemisphere from 12,900 to
646 11,700 cal BP (Rasmussen et al., 2014). As previously mentioned for the B/A, several studies
647 (Renssen and Isarin, 2001; Heiri et al., 2014; Moreno et al., 2014) suggest that temperatures
648 during the YD are less contrasted in the South of Europe in comparison with the North. In Italy
649 as a whole (Fig. 9), a decline in temperatures is recorded in all records. At Matese, a decrease
650 of temperatures is evidenced by the pollen-based reconstructions, but it is less clear from the
651 brGDGT-based reconstructions. The difference of climate signals may be related to different
652 sources between both proxies. Pollen record local, extra-local and regional vegetation
653 (Jacobson and Bradshaw, 1981). The basin size of the Lake Matese is larger than 5 hectares,
654 which suggest a signal of regional vegetation rather than local (Jacobson and Bradshaw, 1981).
655 Moreover, the YD is marked by a large proportion of herbaceous taxa (Fig. 4) and favors the
656 catching of regional pollen (Jacobson and Bradshaw, 1981). On the contrary, brGDGTs are
657 produced in the lake or in the catchment area (Russell et al., 2018; Martin et al., 2019) and thus
658 are local contributors. Moreover, the YD is characterized by high erosion rates in the catchment
659 (Fig. 4), which could favor greater soil-derived brGDGTs and induce a warm bias in
660 temperatures (Martínez-Sosa et al., 2021). At Monticchio (Fig. 9I), contrasted trends are also
661 recorded by the three different climate variables used for pollen-based temperature
662 reconstructions: a decrease in winter temperature is reconstructed for two lake cores, while a
663 fen core external to the lake, which should record the local vegetation signal, does not reveal
664 the temperature decline during the YD (Allen et al., 2002). However, the two other cores clearly
665 show a temperature decrease, that is why we consider a winter temperature decrease during the
666 YD at Monticchio. In Southern Italian records, temperature reconstructions based on alkenones,
667 foraminifera and pollen (Sbaffi et al., 2004; Desprat et al., 2013; Sicre et al., 2013) show a
668 shorter YD than in the north. For alkenones-based reconstructions, even an increase of
669 temperatures is recorded at the end of the YD. In continental records of South Italy (Allen et
670 al., 2002), this trend is only recorded at Monticchio (one core only) and does not appears at
671 Matese. Nonetheless, this hypothesis is only based on marine records and should be investigated
672 through continental records in Southern Italy. In terms of precipitation, the marine cores located
673 south of latitude 42°N record a slight temperature increase based on pollen (Fig. 9GH;
674 Combourieu-Nebout et al., 2013) and $\delta^{18}\text{O}$ *G. bulloides* data (Fig. 9FI; Sicre et al., 2013).
675 However, no significant change occurs at Matese for PANN (Fig. 10D), and on the contrary a
676 low decline is recorded for P_{winter} towards the end of the YD (Fig. 10E). Above latitude 42°N,



677 a precipitation decrease during the YD is recorded by two sites at Hölloch and Corchia caves
678 (Fig. 10BC; Regattieri et al., 2014; Li et al., 2021). According to the model outputs of Rea et
679 al. (2020), drier conditions occurred in Northern Europe whereas wetter conditions prevailed in
680 Southern Europe, mainly during winter and in the South of Italy, the Dinaric Alps and Northern
681 Turkey. This pattern is consistent with our reconstruction but the limit between the North and
682 the South is closer to latitude 42°N.

683 The transition between the YD and the Holocene is recorded around 11,700 cal BP by
684 Greenland ice-core records (Rasmussen et al., 2014). In Italy, an important increase of
685 temperature is recorded in all records (Fig. 9) which appears earlier (700-400 years) in southern
686 sites (Sbaffi et al., 2004; Sicre et al., 2013). In terms of precipitation, marine records south of
687 latitude 42°N continue to record a slight increase of precipitation (Fig. 10F-I; Combourieu-
688 Nebout et al., 2013; Sicre et al., 2013), and in northern sites an abrupt increase of precipitation
689 is recorded (Fig. 10B-E; Regattieri et al., 2014; Li et al., 2021; this study).

690

691 5.4 Atmospheric processes during the Lateglacial in central Mediterranean

692 According to several studies, climate changes during the Lateglacial show differences
693 in temperatures between Southern and Central Europe (Heiri et al., 2014; Moreno et al., 2014;
694 Renssen and Isarin, 2001). In Italy (Fig. 9), climate reconstructions do not show latitudinal
695 differences in terms of temperature. The B/A is marked by warm conditions and the YD by cold
696 conditions even in Southern Italy. Climate reconstructions of Heiri et al., (2014) are not
697 consistent with our results probably because (1) they are based only on two chironomid records
698 located in North Italy, (2) they do not include records from Central and South of Italy, and (3)
699 their reconstructions are also influenced by a record from Bulgaria which can potentially biased
700 the signal of Southern Europe. In the study of Moreno et al. (2014), only the record of
701 Monticchio is used for the South of Italy during the Lateglacial, which may explain the
702 differences in our study. Considering precipitation, several studies suggest no significant
703 changes during the B/A but drier conditions in Northern Europe and wetter conditions in
704 Southern Europe during the YD. In Italy (Fig. 10), we observe the same dynamics during the
705 B/A and the YD.

706 Several studies (Renssen and Isarin, 2001; Moreno et al., 2014; Rea et al., 2020) explain
707 that during cold periods of the Lateglacial (OD, YD) the Polar Frontal JetStream moved
708 southward with a weak Atlantic Meridional Overturning Circulation (AMOC) (Moreno et al.,
709 2014; Rea et al., 2020; Renssen and Isarin, 2001). The incursion of cold air masses is recorded
710 until the South of Italy, however, during the YD, dry conditions are not reconstructed in this



711 region. According to Rea et al. (2020), a relocation of Atlantic storm tracks into the
712 Mediterranean is induced by the Fennoscandian ice sheet and the North European Plain which
713 created a topographic barrier and a high pressure region during the YD. The presence of Atlantic
714 storm tracks into the Mediterranean could have favored wetter conditions in the South of Italy
715 during the YD. Our study suggests a limit around latitude 42°N with drier conditions in
716 Northern Italy and slightly wetter conditions in Southern Italy during the YD. A latitude limit
717 at 40°N was previously discussed by Magny et al. (2013) for the Holocene. These echoing
718 limits over time in Italy inevitably reinforce Italy's key position to archive proxies catching
719 atmospheric patterns.

720 On the contrary, during the B/A, the North Atlantic sea-ice has a more northerly position
721 inducing a northward shift of the Polar Frontal JetStream (Renssen and Isarin, 2001). The
722 incursion of warm air masses is recorded in all of Italy, however, no significant changes in
723 annual precipitation occur. Our study does not suggest the location of Atlantic storm tracks in
724 Italy during the B/A, although at Matese winter precipitation was higher in most pollen-based
725 climate reconstructions. However, very few records and climatic models reconstructing
726 precipitation are available in Europe and the Mediterranean region for this period. Further
727 investigations are necessary to fully understand the atmospheric processes and precipitation
728 dynamic in Europe, mainly during the B/A.

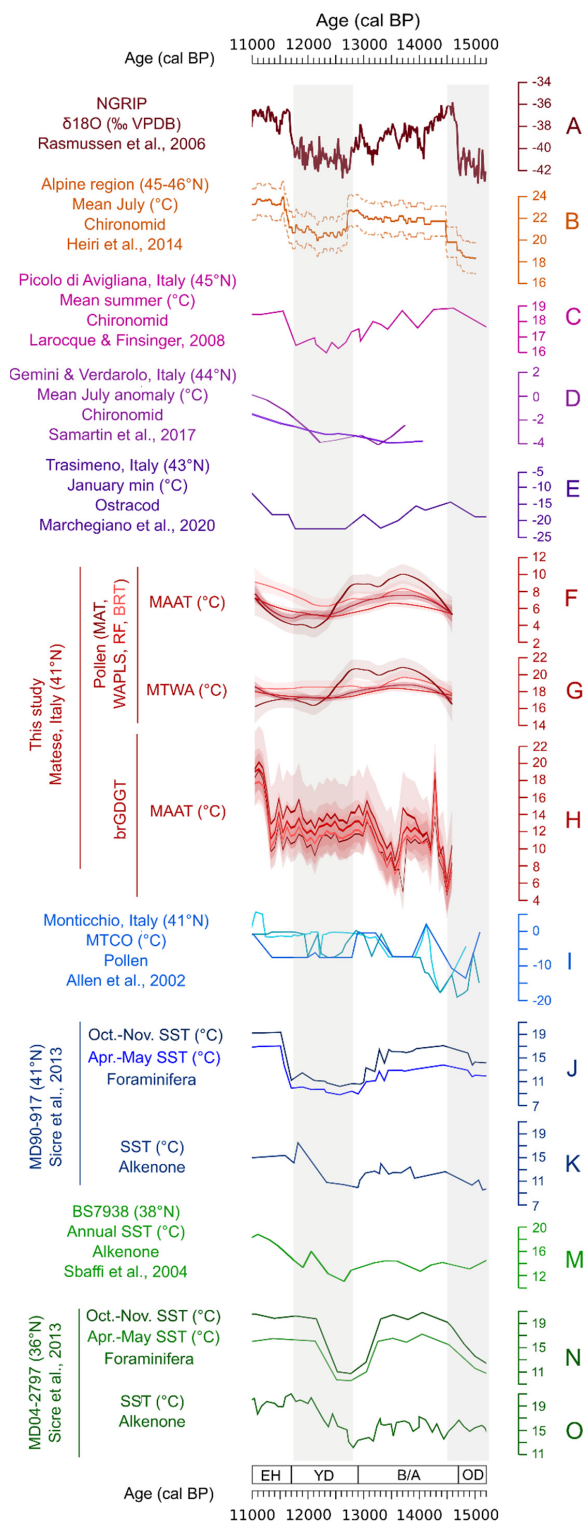
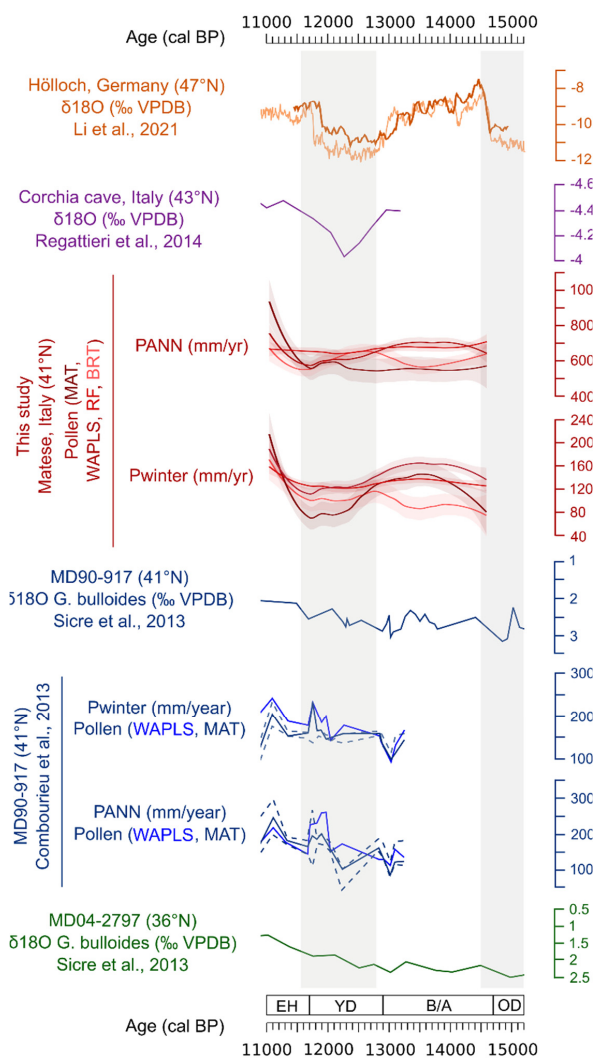




Figure 9. Synthesis of temperature records inferred from different proxies in Italy from 15,000 to 11,000 cal BP and comparison with the NGRIP ice core record. MAAT: mean annual air temperature. MTWA: mean temperature of the warmest month. MTCO: mean temperature of the coldest month. OD: Oldest Dryas. B/A: Bølling–Allerød. YD: Younger Dryas. EH: Early Holocene.

730



731

Figure 10. Synthesis of precipitation records inferred from different proxies in Italy 15,000 to 11,000 cal BP. PANN: mean annual precipitation. P_{winter}: winter precipitation. OD: Oldest Dryas. B/A: Bølling–Allerød. YD: Younger Dryas. EH: Early Holocene.

732



733 6. Conclusions

734 This study provides a quantitative climate reconstruction for the Lateglacial period in
735 South Central Europe, inferred from a multi-proxy and multi-method approach based on the
736 Lake Matese record. The comparison of the Lake Matese climate reconstructions based on
737 brGDGTs and pollen and their comparison with regional terrestrial/marine climate
738 reconstructions show the following:

- 739 • For the first time, pollen and brGDGTs were combined to reconstruct climate
740 changes in the Mediterranean region during the Lateglacial. Temperature trends
741 reconstructed with these proxies are consistent except during the YD. Both proxies
742 show a marked cold OD, an increase of temperatures during the B/A, and an abrupt
743 transition to warmer conditions for the Holocene. During the YD, pollen-based
744 reconstructions show a decrease of temperatures, whereas brGDGT-based
745 reconstructions show no significant changes.
- 746 • Comparison with regional climate records of Italy reveals that there are no
747 latitudinal differences during the B/A and the YD in terms of temperatures. The B/A
748 is marked by an increase of temperature and the YD is characterized by cold
749 conditions in all Italy. On the contrary, precipitation does not show changes during
750 the B/A, and a slight increase of precipitation during the YD is recorded in Southern
751 Italy below latitude 42°N.
- 752 • Cold conditions during the YD in Italy may be linked to the southward position of
753 North Atlantic sea-ice and of the Polar Frontal JetStream. The low increase of
754 precipitation during the YD may be linked to relocation of Atlantic storm tracks into
755 the Mediterranean, induced by the Fennoscandian ice sheet and the North European
756 Plain. We identified the latitude 42°N as a limit between dry conditions in northern
757 Italy and slightly wetter conditions in Southern Italy during the YD. On the contrary,
758 warm conditions during the B/A may be linked to the northward position of North
759 Atlantic sea-ice and of the Polar Frontal JetStream.

760
761 In summary, this study allowed us to document and discuss past climate changes in Italy
762 while contributing to the debate about the atmospheric processes in Southern Europe. The
763 latitudes 40-42°N appear as a key junction point between wetter conditions in Southern Italy
764 and drier conditions in Northern Italy during the YD but also during the Early-Mid Holocene
765 (Magny et al., 2013). However, further robust paleoclimate studies are needed to provide 1)
766 high-resolution reconstructions based on several proxies in Northern Italy, 2) new records for



767 central Italy (between 41-43°N), 3) new continental records for Southern Italy (below 41°N)
768 and 4) more model outputs at regional scales with transient simulations, if possible, mainly
769 during the B/A and the YD.

770

771 **Author contribution**

772 MR: Conceptualization, Field work, Laboratory work, Formal analysis, Writing draft
773 manuscript, Review, Funding acquisition. SJ, OP and EB: Conceptualization, Field work,
774 Supervision, Review, Funding acquisition. GM: Conceptualization, Supervision, Review,
775 Funding acquisition. SW: Laboratory work, Formal analysis, Review, Funding acquisition. OA
776 and MB: Laboratory work. BV: Supervision of laboratory work, Review. BP: Field work. SAA:
777 Coordination of laboratory work. LC and SG: Conceptualization, Review. J-LB, LD and AC:
778 Review.

779

780 **Declaration of competing interest**

781 The authors declare that they have no known competing financial interests or personal
782 relationships that could have appeared to influence the work reported in this paper.

783

784 **Funding**

785 This research was co-funded by the International PhD course “Agriculture
786 Technologies and Biotechnologies” (34° Cycle, Code: DOT1339335). Financial support for
787 this study was provided by EFFICACE project from EC2CO INSU CNRS (PI: Odile Peyron)
788 and ERJ ClimMatese from LabEx CeMEB (PI: Mary Robles). The travels between Italy and
789 France were financed by VINCI founding of the Università Italo Francese (UIF). The
790 conference funding was provided by the Association des Palynologues de Langue Française
791 (APLF).

792

793 **Acknowledgements**

794 The authors would like to thank Julien Didier for magnetic susceptibility measurements,
795 Laurent Bouby and Isabelle Figueral for seed and wood identifications used for radiocarbon
796 dating. The authors would like to express their appreciation to Gwenaël Magne, Thierry Pastor
797 and Benoît Brossier for logistical support during fieldwork, and Anne-Lise Develle and Claire
798 Blanchet for help during XRF analysis. We would like to thank Sandrine Canal and Sylvie



799 Rouland for support during pollen sample preparation. This is an ISEM contribution N° XXXX-
800 XXX.

801

802 References

- 803 Allen, J.R.M., Watts, W.A., McGee, E., Huntley, B., 2002. Holocene environmental variability-
804 the record from Lago Grande di Monticchio, Italy. *Quaternary International* 88, 69–80.
- 805 Ammann, B., Birks, H.J.B., Brooks, S.J., Eicher, U., von Grafenstein, U., Hofmann, W.,
806 Lemdahl, G., Schwander, J., Tobolski, K., Wick, L., 2000. Quantification of biotic
807 responses to rapid climatic changes around the Younger Dryas — a synthesis.
808 *Palaeogeography, Palaeoclimatology, Palaeoecology* 159, 313–347.
809 [https://doi.org/10.1016/S0031-0182\(00\)00092-4](https://doi.org/10.1016/S0031-0182(00)00092-4)
- 810 Aucelli, P.P.C., Cesarano, M., Di Paola, G., Filocamo, F., Roskopf, C.M., 2013.
811 Geomorphological map of the central sector of the Matese Mountains (Southern Italy):
812 an example of complex landscape evolution in a Mediterranean mountain environment.
813 *Journal of Maps* 9, 604–616. <https://doi.org/10.1080/17445647.2013.840054>
- 814 Barton, C.M., Aura Tortosa, J.E., Garcia-Puchol, O., Riel-Salvatore, J.G., Gauthier, N., Vadillo
815 Conesa, M., Pothier Bouchard, G., 2018. Risk and resilience in the late glacial: A case
816 study from the western Mediterranean. *Quaternary Science Reviews* 184, 68–84.
817 <https://doi.org/10.1016/j.quascirev.2017.09.015>
- 818 Beug, H.-J., 2004. Leitfaden der Pollenbestimmung für Mitteleuropa und angrenzende Gebiete.
819 Friedrich Pfeil, München.
- 820 Blaauw, M., 2010. Methods and code for ‘classical’ age-modelling of radiocarbon sequences.
821 *Quaternary Geochronology* 5, 512–518. <https://doi.org/10.1016/j.quageo.2010.01.002>
- 822 Blaga, C.I., Reichert, G.-J., Lotter, A.F., Anselmetti, F.S., Sinninghe Damsté, J.S., 2013. A
823 TEX₈₆ lake record suggests simultaneous shifts in temperature in Central Europe and
824 Greenland during the last deglaciation: A SWISS TEX₈₆ LAKE RECORD. *Geophys.*
825 *Res. Lett.* 40, 948–953. <https://doi.org/10.1002/grl.50181>
- 826 Breiman, L., 2001. Random Forests. *Machine Learning* 45, 5–32.
827 <https://doi.org/10.1023/A:1010933404324>
- 828 Bronk Ramsey, C., Albert, P.G., Blockley, S.P.E., Hardiman, M., Housley, R.A., Lane, C.S.,
829 Lee, S., Matthews, I.P., Smith, V.C., Lowe, J.J., 2015. Improved age estimates for key
830 Late Quaternary European tephra horizons in the RESET lattice. *Quaternary Science*
831 *Reviews* 118, 18–32. <https://doi.org/10.1016/j.quascirev.2014.11.007>
- 832 Carranza, M.L., Frate, L., Paura, B., 2012. Structure, ecology and plant richness patterns in
833 fragmented beech forests. *Plant Ecology & Diversity* 5, 541–551.
834 <https://doi.org/10.1080/17550874.2012.740509>
- 835 Castañeda, I.S., Schouten, S., 2011. A review of molecular organic proxies for examining
836 modern and ancient lacustrine environments. *Quaternary Science Reviews* 30, 2851–
837 2891. <https://doi.org/10.1016/j.quascirev.2011.07.009>
- 838 Chevalier, M., Davis, B.A.S., Heiri, O., Seppä, H., Chase, B.M., Gajewski, K., Lacourse, T.,
839 Telford, R.J., Finsinger, W., Guiot, J., Kühl, N., Maezumi, S.Y., Tipton, J.R., Carter,
840 V.A., Brussel, T., Phelps, L.N., Dawson, A., Zanon, M., Vallé, F., Nolan, C., Mauri, A.,
841 de Vernal, A., Izumi, K., Holmström, L., Marsicek, J., Goring, S., Sommer, P.S.,
842 Chaput, M., Kupriyanov, D., 2020. Pollen-based climate reconstruction techniques for
843 late Quaternary studies. *Earth-Science Reviews* 210, 103384.
844 <https://doi.org/10.1016/j.earscirev.2020.103384>
- 845 Combourieu-Nebout, N., Peyron, O., Bout-Roumazeilles, V., Goring, S., Dormoy, I., Joannin,
846 S., Sadori, L., Siani, G., Magny, M., 2013. Holocene vegetation and climate changes in



- 847 the central Mediterranean inferred from a high-resolution marine pollen record (Adriatic
848 Sea). *Clim. Past* 9, 2023–2042. <https://doi.org/10.5194/cp-9-2023-2013>
- 849 Coope, G.R., Lemdahl, G., 1995. Regional differences in the Lateglacial climate of northern
850 Europe based on coleopteran analysis. *Journal of Quaternary Science* 10, 391–395.
851 <https://doi.org/10.1002/jqs.3390100409>
- 852 Davtian, N., Bard, E., Ménot, G., Fagault, Y., 2018. The importance of mass accuracy in
853 selected ion monitoring analysis of branched and isoprenoid tetraethers. *Organic*
854 *Geochemistry* 118, 58–62. <https://doi.org/10.1016/j.orggeochem.2018.01.007>
- 855 De Beaulieu, J.-L., Brugiapaglia, E., Joannin, S., Guiter, F., Zanchetta, G., Wulf, S., Peyron,
856 O., Bernardo, L., Didier, J., Stock, A., Rius, D., Magny, M., 2017. Lateglacial-Holocene
857 abrupt vegetation changes at Lago Trifoglietti in Calabria, Southern Italy: The setting
858 of ecosystems in a refugial zone. *Quaternary Science Reviews* 158, 44–57.
859 <https://doi.org/10.1016/j.quascirev.2016.12.013>
- 860 De Jonge, C., Stadnitskaia, A., Hopmans, E.C., Cherkashov, G., Fedotov, A., Sinninghe
861 Damsté, J.S., 2014. In situ produced branched glycerol dialkyl glycerol tetraethers in
862 suspended particulate matter from the Yenisei River, Eastern Siberia. *Geochimica et*
863 *Cosmochimica Acta* 125, 476–491. <https://doi.org/10.1016/j.gca.2013.10.031>
- 864 Dearing Crampton-Flood, E., Tierney, J.E., Peterse, F., Kirkels, F.M.S.A., Sinninghe Damsté,
865 J.S., 2020. BayMBT: A Bayesian calibration model for branched glycerol dialkyl
866 glycerol tetraethers in soils and peats. *Geochimica et Cosmochimica Acta* 268, 142–
867 159. <https://doi.org/10.1016/j.gca.2019.09.043>
- 868 De'ath, G., 2007. Boosted trees for ecological modeling and prediction. *Ecology* 88, 243–251.
869 [https://doi.org/10.1890/0012-9658\(2007\)88\[243:BTFEMA\]2.0.CO;2](https://doi.org/10.1890/0012-9658(2007)88[243:BTFEMA]2.0.CO;2)
- 870 Desprat, S., Combourieu-Nebout, N., Essallami, L., Sicre, M.A., Dormoy, I., Peyron, O., Siani,
871 G., Bout Roumazeilles, V., Turon, J.L., 2013. Deglacial and Holocene vegetation and
872 climatic changes in the southern Central Mediterranean from a direct land–sea
873 correlation. *Clim. Past* 9, 767–787. <https://doi.org/10.5194/cp-9-767-2013>
- 874 Ding, S., Schwab, V.F., Ueberschaar, N., Roth, V.-N., Lange, M., Xu, Y., Gleixner, G., Pohnert,
875 G., 2016. Identification of novel 7-methyl and cyclopentanyl branched glycerol dialkyl
876 glycerol tetraethers in lake sediments. *Organic Geochemistry* 102, 52–58.
877 <https://doi.org/10.1016/j.orggeochem.2016.09.009>
- 878 Drescher-Schneider, R., de Beaulieu, J.-L., Magny, M., Walter-Simonnet, A.-V., Bossuet, G.,
879 Millet, L., Brugiapaglia, E., Drescher, A., 2007. Vegetation history, climate and human
880 impact over the last 15,000 years at Lago dell'Accesa (Tuscany, Central Italy). *Veget*
881 *Hist Archaeobot* 16, 279–299. <https://doi.org/10.1007/s00334-006-0089-z>
- 882 Dugerdil, L., Joannin, S., Peyron, O., Jouffroy-Bapicot, I., Vannière, B., Boldgiv, B.,
883 Unkelbach, J., Behling, H., Ménot, G., 2021a. Climate reconstructions based on GDGT
884 and pollen surface datasets from Mongolia and Baikal area: calibrations and
885 applicability to extremely cold–dry environments over the Late Holocene. *Clim. Past*
886 17, 1199–1226. <https://doi.org/10.5194/cp-17-1199-2021>
- 887 Dugerdil, L., Ménot, G., Peyron, O., Jouffroy-Bapicot, I., Ansanay-Alex, S., Antheaume, I.,
888 Behling, H., Boldgiv, B., Develle, A.-L., Grossi, V., Magail, J., Makou, M., Robles, M.,
889 Unkelbach, J., Vannière, B., Joannin, S., 2021b. Late Holocene Mongolian climate and
890 environment reconstructions from brGDGTs, NPPs and pollen transfer functions for
891 Lake Ayrag: Paleoclimate implications for Arid Central Asia. *Quaternary Science*
892 *Reviews* 273, 107235. <https://doi.org/10.1016/j.quascirev.2021.107235>
- 893 Duprat-Oualid, F., Bégeot, C., Peyron, O., Rius, D., Millet, L., Magny, M., 2022. High-
894 frequency vegetation and climatic changes during the Lateglacial inferred from the
895 Lapsou pollen record (Cantal, southern Massif Central, France). *Quaternary*
896 *International* S1040618222001537. <https://doi.org/10.1016/j.quaint.2022.04.012>



- 897 Elith, J., Leathwick, J.R., Hastie, T., 2008. A working guide to boosted regression trees. *J Anim*
898 *Ecology* 77, 802–813. <https://doi.org/10.1111/j.1365-2656.2008.01390.x>
- 899 Faegri, K., Kaland, P.E., Krzywinski, K., 1989. *Textbook of pollen analysis*. John Wiley &
900 Sons, Chichester.
- 901 Ferranti, L., Milano, G., Burrato, P., Palano, M., Cannavò, F., 2015. The seismogenic structure
902 of the 2013–2014 Matese seismic sequence, Southern Italy: implication for the
903 geometry of the Apennines active extensional belt. *Geophysical Journal International*
904 201, 823–837. <https://doi.org/10.1093/gji/ggv053>
- 905 Ferrarini, F., Boncio, P., de Nardis, R., Pappone, G., Cesarano, M., Aucelli, P.P.C., Lavecchia,
906 G., 2017. Segmentation pattern and structural complexities in seismogenic extensional
907 settings: The North Matese Fault System (Central Italy). *Journal of Structural Geology*
908 95, 93–112. <https://doi.org/10.1016/j.jsg.2016.11.006>
- 909 Finsinger, W., Heiri, O., Valsecchi, V., Tinner, W., Lotter, A.F., 2007. Modern pollen
910 assemblages as climate indicators in southern Europe. *Global Ecology and*
911 *Biogeography* 16, 567–582. <https://doi.org/10.1111/j.1466-8238.2007.00313.x>
- 912 Fiorillo, F., Doglioni, A., 2010. The relation between karst spring discharge and rainfall by
913 cross-correlation analysis (Campania, southern Italy). *Hydrogeol J* 18, 1881–1895.
914 <https://doi.org/10.1007/s10040-010-0666-1>
- 915 Fiorillo, F., Pagnozzi, M., 2015. Recharge processes of Matese karst massif (southern Italy).
916 *Environ Earth Sci* 74, 7557–7570. <https://doi.org/10.1007/s12665-015-4678-y>
- 917 Galli, P., Giaccio, B., Messina, P., Peronace, E., Amato, V., Naso, G., Nomade, S., Pereira, A.,
918 Piscitelli, S., Bellanova, J., Billi, A., Blamart, D., Galderisi, A., Giocoli, A., Stabile, T.,
919 Thil, F., 2017. Middle to Late Pleistocene activity of the northern Matese fault system
920 (southern Apennines, Italy). *Tectonophysics* 699, 61–81.
921 <https://doi.org/10.1016/j.tecto.2017.01.007>
- 922 Gandouin, E., Rioual, P., Pailles, C., Brooks, S.J., Ponel, P., Guiter, F., Djamali, M., Andrieu-
923 Ponel, V., Birks, H.J.B., Leydet, M., Belkacem, D., Haas, J.N., Van der Putten, N., de
924 Beaulieu, J.L., 2016. Environmental and climate reconstruction of the late-glacial-
925 Holocene transition from a lake sediment sequence in Aubrac, French Massif Central:
926 Chironomid and diatom evidence. *Palaeogeography, Palaeoclimatology, Palaeoecology*
927 461, 292–309. <https://doi.org/10.1016/j.palaeo.2016.08.039>
- 928 Guarino, R., Bazan, G., Paura, B., 2015. Downy-Oak Woods of Italy: Phytogeographical
929 Remarks on a Controversial Taxonomic and Ecologic Issue, in: Box, E.O., Fujiwara, K.
930 (Eds.), *Warm-Temperate Deciduous Forests around the Northern Hemisphere*,
931 *Geobotany Studies*. Springer International Publishing, Cham, pp. 139–151.
932 https://doi.org/10.1007/978-3-319-01261-2_7
- 933 Guiot, J., 1990. Methodology of the last climatic cycle reconstruction in France from pollen
934 data. *Palaeogeography, Palaeoclimatology, Palaeoecology, Methods for the Study of*
935 *Stratigraphical Records* 80, 49–69. [https://doi.org/10.1016/0031-0182\(90\)90033-4](https://doi.org/10.1016/0031-0182(90)90033-4)
- 936 Guiot, J., de Beaulieu, J.L., Cheddadi, R., David, F., Ponel, P., Reille, M., 1993. The climate in
937 Western Europe during the last Glacial/Interglacial cycle derived from pollen and insect
938 remains. *Palaeogeography, Palaeoclimatology, Palaeoecology* 103, 73–93.
939 [https://doi.org/10.1016/0031-0182\(93\)90053-L](https://doi.org/10.1016/0031-0182(93)90053-L)
- 940 Heiri, O., Brooks, S.J., Renssen, H., Bedford, A., Hazekamp, M., Ilyashuk, B., Jeffers, E.S.,
941 Lang, B., Kirilova, E., Kuiper, S., Millet, L., Samartin, S., Toth, M., Verbruggen, F.,
942 Watson, J.E., van Asch, N., Lammertsma, E., Amon, L., Birks, H.H., Birks, H.J.B.,
943 Mortensen, M.F., Hoek, W.Z., Magyari, E., Muñoz Sobrino, C., Seppä, H., Tinner, W.,
944 Tonkov, S., Veski, S., Lotter, A.F., 2014. Validation of climate model-inferred regional
945 temperature change for late-glacial Europe. *Nat Commun* 5, 4914.
946 <https://doi.org/10.1038/ncomms5914>



- 947 Heiri, O., Ilyashuk, B., Millet, L., Samartin, S., Lotter, A.F., 2015. Stacking of discontinuous
948 regional palaeoclimate records: Chironomid-based summer temperatures from the
949 Alpine region. *The Holocene* 25, 137–149. <https://doi.org/10.1177/0959683614556382>
- 950 Hepp, J., Wüthrich, L., Bromm, T., Bliedtner, M., Schäfer, I.K., Glaser, B., Rozanski, K.,
951 Sirocko, F., Zech, R., Zech, M., 2019. How dry was the Younger Dryas? Evidence from
952 a coupled $\delta^2\text{H}$ – $\delta^{18}\text{O}$ biomarker paleohygrometer applied to the Gemündener Maar
953 sediments, Western Eifel, Germany. *Climate of the Past* 15, 713–733.
954 <https://doi.org/10.5194/cp-15-713-2019>
- 955 Hijmans, R.J., Phillips, S., Elith, J.L. and J., 2021. *dismo: Species Distribution Modeling*.
- 956 Hopmans, E.C., Schouten, S., Sinninghe Damsté, J.S., 2016. The effect of improved
957 chromatography on GDGT-based palaeoproxies. *Organic Geochemistry* 93, 1–6.
958 <https://doi.org/10.1016/j.orggeochem.2015.12.006>
- 959 Huguet, C., Hopmans, E.C., Febo-Ayala, W., Thompson, D.H., Sinninghe Damsté, J.S.,
960 Schouten, S., 2006. An improved method to determine the absolute abundance of
961 glycerol dibiphytanyl glycerol tetraether lipids. *Organic Geochemistry* 37, 1036–1041.
962 <https://doi.org/10.1016/j.orggeochem.2006.05.008>
- 963 Hunt, J.B., Hill, P.G., 1996. An inter-laboratory comparison of the electron probe microanalysis
964 of glass geochemistry. *Quaternary International* 34–36, 229–241.
965 [https://doi.org/10.1016/1040-6182\(95\)00088-7](https://doi.org/10.1016/1040-6182(95)00088-7)
- 966 Jacobson, G.L., Bradshaw, R.H.W., 1981. The Selection of Sites for Paleovegetational Studies.
967 *Quat. res.* 16, 80–96. [https://doi.org/10.1016/0033-5894\(81\)90129-0](https://doi.org/10.1016/0033-5894(81)90129-0)
- 968 Joannin, S., Brugiapaglia, E., Vanniere, B., 2012. Pollen-based reconstruction of Holocene
969 vegetation and climate in southern Italy: the case of Lago Trifoglietti. *Clim. Past* 24.
- 970 Jochum, K.P., Stoll, B., Herwig, K., Willbold, M., Hofmann, A.W., Amini, M., Aarburg, S.,
971 Abouchami, W., Hellebrand, E., Mocek, B., Raczek, I., Stracke, A., Alard, O., Bouman,
972 C., Becker, S., Dücking, M., Brätz, H., Klemd, R., de Bruin, D., Canil, D., Cornell, D.,
973 de Hoog, C.-J., Dalpé, C., Danyushevsky, L., Eisenhauer, A., Gao, Y., Snow, J.E.,
974 Groschopf, N., Günther, D., Latkoczy, C., Guillong, M., Hauri, E.H., Höfer, H.E.,
975 Lahaye, Y., Horz, K., Jacob, D.E., Kasemann, S.A., Kent, A.J.R., Ludwig, T., Zack, T.,
976 Mason, P.R.D., Meixner, A., Rosner, M., Misawa, K., Nash, B.P., Pfänder, J., Premo,
977 W.R., Sun, W.D., Tiepolo, M., Vannucci, R., Vennemann, T., Wayne, D., Woodhead,
978 J.D., 2006. MPI-DING reference glasses for in situ microanalysis: New reference values
979 for element concentrations and isotope ratios: MPI-DING REFERENCE GLASSES.
980 *Geochem. Geophys. Geosyst.* 7, n/a-n/a. <https://doi.org/10.1029/2005GC001060>
- 981 Juggins, S., Juggins, M.S., 2020. Package ‘rioja.’
- 982 Kuehn, S.C., Froese, D.G., Shane, P.A.R., 2011. The INTAV intercomparison of electron-beam
983 microanalysis of glass by tephrochronology laboratories: Results and recommendations.
984 *Quaternary International, Enhancing tephrochronology and its application (INTREPID
985 Project): Hiroshi Machida commemorative volume* 246, 19–47.
986 <https://doi.org/10.1016/j.quaint.2011.08.022>
- 987 Larocque, I., Finsinger, W., 2008. Late-glacial chironomid-based temperature reconstructions
988 for Lago Piccolo di Avigliana in the southwestern Alps (Italy). *Palaeogeography,
989 Palaeoclimatology, Palaeoecology* 257, 207–223.
990 <https://doi.org/10.1016/j.palaeo.2007.10.021>
- 991 Li, H., Spötl, C., Cheng, H., 2021. A high-resolution speleothem proxy record of the Late
992 Glacial in the European Alps: extending the NALPS19 record until the beginning of the
993 Holocene. *J. Quaternary Sci* 36, 29–39. <https://doi.org/10.1002/jqs.3255>
- 994 Liaw, A., Wiener, M., 2002. *Classification and Regression by randomForest* 2, 5.
- 995 Lotter, A.F., Heiri, O., Brooks, S., van Leeuwen, J.F.N., Eicher, U., Ammann, B., 2012. Rapid
996 summer temperature changes during Termination 1a: high-resolution multi-proxy



- 997 climate reconstructions from Gerzensee (Switzerland). *Quaternary Science Reviews*,
998 The INTegration of Ice core, Marine and TERrestrial records of the last termination
999 (INTIMATE) 60,000 to 8000 BP 36, 103–113.
1000 <https://doi.org/10.1016/j.quascirev.2010.06.022>
- 1001 Magny, M., Combourieu-Nebout, N., de Beaulieu, J.-L., Bout-Roumazielles, V., Colombaroli,
1002 D., Desprat, S., Francke, A., Joannin, S., Ortu, E., Peyron, O., Revel, M., Sadori, L.,
1003 Siani, G., Sicre, M.A., Samartin, S., Simonneau, A., Tinner, W., Vanniere, B., Wagner,
1004 B., Zanchetta, G., Anselmetti, F., Brugiapaglia, E., Chapron, E., Debret, M., Didier, J.,
1005 Essallami, L., Galop, D., Gilli, A., Kallel, N., Millet, L., Stock, A., Turon, J.L., Wirth,
1006 S., 2013. North-south palaeohydrological contrasts in the central Mediterranean during
1007 the Holocene: tentative synthesis and working hypotheses. *Clim. Past* 30.
- 1008 Marchegiano, M., Horne, D.J., Gliozzi, E., Francke, A., Wagner, B., Ariztegui, D., 2020. Rapid
1009 Late Pleistocene climate change reconstructed from a lacustrine ostracod record in
1010 central Italy (Lake Trasimeno, Umbria). *Boreas* 49, 739–750.
1011 <https://doi.org/10.1111/bor.12450>
- 1012 Martin, C., Ménot, G., Thouveny, N., Davtian, N., Andrieu-Ponel, V., Reille, M., Bard, E.,
1013 2019. Impact of human activities and vegetation changes on the tetraether sources in
1014 Lake St Front (Massif Central, France). *Organic Geochemistry* 135, 38–52.
- 1015 Martin, C., Ménot, G., Thouveny, N., Peyron, O., Andrieu-Ponel, V., Montade, V., Davtian,
1016 N., Reille, M., Bard, E., 2020. Early Holocene Thermal Maximum recorded by branched
1017 tetraethers and pollen in Western Europe (Massif Central, France). *Quaternary Science*
1018 *Reviews* 228, 106109. <https://doi.org/10.1016/j.quascirev.2019.106109>
- 1019 Martínez-Sosa, P., Tierney, J.E., Stefanescu, I.C., Dearing Crampton-Flood, E., Shuman, B.N.,
1020 Routson, C., 2021. A global Bayesian temperature calibration for lacustrine brGDGTs.
1021 *Geochimica et Cosmochimica Acta* 305, 87–105.
1022 <https://doi.org/10.1016/j.gca.2021.04.038>
- 1023 Mercuri, A.M., Accorsi, C.A., Bandini Mazzanti, M., 2002. The long history of Cannabis and
1024 its cultivation by the Romans in central Italy, shown by pollen records from Lago
1025 Albano and Lago di Nemi. *Veget Hist Archaeobot* 11, 263–276.
1026 <https://doi.org/10.1007/s003340200039>
- 1027 Millet, L., Rius, D., Galop, D., Heiri, O., Brooks, S.J., 2012. Chironomid-based reconstruction
1028 of Lateglacial summer temperatures from the Ech palaeolake record (French western
1029 Pyrenees). *Palaeogeography, Palaeoclimatology, Palaeoecology* 315–316, 86–99.
1030 <https://doi.org/10.1016/j.palaeo.2011.11.014>
- 1031 Moore, P.D., Webb, J.A., Collinson, M.E., 1991. *Pollen Analysis*, Subsequent edition. ed.
1032 Blackwell Science Inc, Oxford.
- 1033 Moreno, A., Svensson, A., Brooks, S.J., Connor, S., Engels, S., Fletcher, W., Genty, D., Heiri,
1034 O., Labuhn, I., Perşoiu, A., Peyron, O., Sadori, L., Valero-Garcés, B., Wulf, S.,
1035 Zanchetta, G., 2014. A compilation of Western European terrestrial records 60–8 ka BP:
1036 towards an understanding of latitudinal climatic gradients. *Quaternary Science Reviews*
1037 106, 167–185. <https://doi.org/10.1016/j.quascirev.2014.06.030>
- 1038 Naafs, B.D.A., Gallego-Sala, A.V., Inglis, G.N., Pancost, R.D., 2017a. Refining the global
1039 branched glycerol dialkyl glycerol tetraether (brGDGT) soil temperature calibration.
1040 *Organic Geochemistry* 106, 48–56. <https://doi.org/10.1016/j.orggeochem.2017.01.009>
- 1041 Naafs, B.D.A., Inglis, G.N., Zheng, Y., Amesbury, M.J., Biester, H., Bindler, R., Blewett, J.,
1042 Burrows, M.A., del Castillo Torres, D., Chambers, F.M., Cohen, A.D., Evershed, R.P.,
1043 Feakins, S.J., Gałka, M., Gallego-Sala, A., Gandois, L., Gray, D.M., Hatcher, P.G.,
1044 Honorio Coronado, E.N., Hughes, P.D.M., Hugué, A., Könönen, M., Laggoun-
1045 Défarge, F., Lähenteoja, O., Lamentowicz, M., Marchant, R., McClymont, E.,
1046 Pontevedra-Pombal, X., Ponton, C., Pourmand, A., Rizzuti, A.M., Rochefort, L.,



- 1047 Schellekens, J., De Vleeschouwer, F., Pancost, R.D., 2017b. Introducing global peat-
1048 specific temperature and pH calibrations based on brGDGT bacterial lipids. *Geochimica*
1049 *et Cosmochimica Acta* 208, 285–301. <https://doi.org/10.1016/j.gca.2017.01.038>
- 1050 Peyron, O., Bégeot, C., Brewer, S., Heiri, O., Magny, M., Millet, L., Ruffaldi, P., Van Campo,
1051 E., Yu, G., 2005. Late-Glacial climatic changes in Eastern France (Lake Lautrey) from
1052 pollen, lake-levels, and chironomids. *Quat. res.* 64, 197–211.
1053 <https://doi.org/10.1016/j.yqres.2005.01.006>
- 1054 Peyron, O., Combourieu-Nebout, N., Brayshaw, D., Goring, S., Andrieu-Ponel, V., Desprat, S.,
1055 Fletcher, W., Gambin, B., Ioakim, C., Joannin, S., Kotthoff, U., Kouli, K., Montade, V.,
1056 Pross, J., Sadori, L., Magny, M., 2017. Precipitation changes in the Mediterranean basin
1057 during the Holocene from terrestrial and marine pollen records: a model–data
1058 comparison. *Clim. Past* 13, 249–265. <https://doi.org/10.5194/cp-13-249-2017>
- 1059 Peyron, O., Goring, S., Dormoy, I., Kotthoff, U., Pross, J., de Beaulieu, J.-L., Drescher-
1060 Schneider, R., Vanni re, B., Magny, M., 2011. Holocene seasonality changes in the
1061 central Mediterranean region reconstructed from the pollen sequences of Lake Accessa
1062 (Italy) and Tenaghi Philippon (Greece). *The Holocene* 21, 131–146.
1063 <https://doi.org/10.1177/0959683610384162>
- 1064 Peyron, O., Guiot, J., Cheddadi, R., Tarasov, P., Reille, M., de Beaulieu, J.-L., Bottema, S.,
1065 Andrieu, V., 1998. Climatic Reconstruction in Europe for 18,000 YR B.P. from Pollen
1066 Data. *Quat. res.* 49, 183–196. <https://doi.org/10.1006/qres.1997.1961>
- 1067 Peyron, O., Magny, M., Goring, S., Joannin, S., de Beaulieu, J.-L., Brugiapaglia, E., Sadori, L.,
1068 Garfi, G., Kouli, K., Ioakim, C., Combourieu-Nebout, N., 2013. Contrasting patterns of
1069 climatic changes during the Holocene across the Italian Peninsula reconstructed from
1070 pollen data. *Clim. Past* 9, 1233–1252. <https://doi.org/10.5194/cp-9-1233-2013>
- 1071 Ponel, P., Guiter, F., Gandouin, E., Peyron, O., de Beaulieu, J.-L., 2022. Late-Glacial
1072 palaeotemperatures and palaeoprecipitations in the Aubrac Mountains (French Massif
1073 Central) reconstructed from multiproxy analyses (Coleoptera, chironomids and pollen).
1074 *Quaternary International*. <https://doi.org/10.1016/j.quaint.2022.02.005>
- 1075 Prasad, A.M., Iverson, L.R., Liaw, A., 2006. Newer Classification and Regression Tree
1076 Techniques: Bagging and Random Forests for Ecological Prediction. *Ecosystems* 9,
1077 181–199. <https://doi.org/10.1007/s10021-005-0054-1>
- 1078 Prentice, C., Guiot, J., Huntley, B., Jolly, D., Cheddadi, R., 1996. Reconstructing biomes from
1079 palaeoecological data: a general method and its application to European pollen data at
1080 0 and 6 ka. *Climate Dynamics* 12, 185–194. <https://doi.org/10.1007/BF00211617>
- 1081 Raberg, J.H., Harning, D.J., Crump, S.E., de Wet, G., Blumm, A., Kopf, S., Geirsd ttir,  .,
1082 Miller, G.H., Sep lveda, J., 2021. Revised fractional abundances and warm-season
1083 temperatures substantially improve brGDGT calibrations in lake sediments.
1084 *Biogeosciences* 18, 3579–3603. <https://doi.org/10.5194/bg-2021-16>
- 1085 Ramos-Rom n, M.J., De Jonge, C., Magyari, E., Veres, D., Ilvonen, L., Develle, A.-L., Sepp ,
1086 H., 2022. Lipid biomarker (brGDGT)- and pollen-based reconstruction of temperature
1087 change during the Middle to Late Holocene transition in the Carpathians. *Global and*
1088 *Planetary Change* 215, 103859. <https://doi.org/10.1016/j.gloplacha.2022.103859>
- 1089 Rasmussen, S.O., Bigler, M., Blockley, S.P., Blunier, T., Buchardt, S.L., Clausen, H.B.,
1090 Cvijanovic, I., Dahl-Jensen, D., Johnsen, S.J., Fischer, H., Gkinis, V., Guillevic, M.,
1091 Hoek, W.Z., Lowe, J.J., Pedro, J.B., Popp, T., Seierstad, I.K., Steffensen, J.P., Svensson,
1092 A.M., Vallenga, P., Vinther, B.M., Walker, M.J.C., Wheatley, J.J., Winstrup, M.,
1093 2014. A stratigraphic framework for abrupt climatic changes during the Last Glacial
1094 period based on three synchronized Greenland ice-core records: refining and extending
1095 the INTIMATE event stratigraphy. *Quaternary Science Reviews* 106, 14–28.
1096 <https://doi.org/10.1016/j.quascirev.2014.09.007>



- 1097 Rea, B.R., Pellitero, R., Spagnolo, M., Hughes, P., Ivy-Ochs, S., Renssen, H., Ribolini, A.,
1098 Bakke, J., Lukas, S., Braithwaite, R.J., 2020. Atmospheric circulation over Europe
1099 during the Younger Dryas. *Sci. Adv.* 6, eaba4844.
1100 <https://doi.org/10.1126/sciadv.aba4844>
- 1101 Regattieri, E., Zanchetta, G., Drysdale, R.N., Isola, I., Hellstrom, J.C., Dallai, L., 2014.
1102 Lateglacial to Holocene trace element record (Ba, Mg, Sr) from Corchia Cave (Apuan
1103 Alps, central Italy): paleoenvironmental implications: Trace element record from
1104 Corchia Cave, central Italy. *J. Quaternary Sci.* 29, 381–392.
1105 <https://doi.org/10.1002/jqs.2712>
- 1106 Rehfeld, K., Münch, T., Ho, S.L., Laepple, T., 2018. Global patterns of declining temperature
1107 variability from the Last Glacial Maximum to the Holocene. *Nature* 554, 356–359.
1108 <https://doi.org/10.1038/nature25454>
- 1109 Reille, M., 1998. Reille, Maurice, 1995. Pollen et spores d’Europe et d’Afrique du Nord,
1110 Supplément 1 . Éditions du Laboratoire de botanique historique et palynologie,
1111 Marseille, 327 p., 800 FF. / Reille, Maurice, 1998. Pollen et spores d’Europe et
1112 d’Afrique du Nord, Supplément 2 . Éditions du Laboratoire de botanique historique et
1113 palynologie, Marseille, 530 p., 1600 FF. *gpq* 52, 0–0. <https://doi.org/10.7202/004885ar>
- 1114 Reimer, P.J., Austin, W.E.N., Bard, E., Bayliss, A., Blackwell, P.G., Ramsey, C.B., Butzin, M.,
1115 Cheng, H., Edwards, R.L., Friedrich, M., Grootes, P.M., Guilderson, T.P., Hajdas, I.,
1116 Heaton, T.J., Hogg, A.G., Hughen, K.A., Kromer, B., Manning, S.W., Muscheler, R.,
1117 Palmer, J.G., Pearson, C., Plicht, J. van der, Reimer, R.W., Richards, D.A., Scott, E.M.,
1118 Southon, J.R., Turney, C.S.M., Wacker, L., Adolphi, F., Büntgen, U., Capano, M.,
1119 Fahrni, S.M., Fogtmann-Schulz, A., Friedrich, R., Köhler, P., Kudsk, S., Miyake, F.,
1120 Olsen, J., Reinig, F., Sakamoto, M., Sookdeo, A., Talamo, S., 2020. The IntCal20
1121 Northern Hemisphere Radiocarbon Age Calibration Curve (0–55 cal kBP). *Radiocarbon*
1122 62, 725–757. <https://doi.org/10.1017/RDC.2020.41>
- 1123 Renssen, H., Isarin, R.F.B., 2001. The two major warming phases of the last deglaciation at
1124 ~14.7 and ~11.5 ka cal BP in Europe: climate reconstructions and AGCM experiments.
1125 *Global and Planetary Change* 30, 117–153. [https://doi.org/10.1016/S0921-](https://doi.org/10.1016/S0921-8181(01)00082-0)
1126 [8181\(01\)00082-0](https://doi.org/10.1016/S0921-8181(01)00082-0)
- 1127 Renssen, H., Mairesse, A., Goosse, H., Mathiot, P., Heiri, O., Roche, D.M., Nisancioglu, K.H.,
1128 Valdes, P.J., 2015. Multiple causes of the Younger Dryas cold period. *Nature Geosci* 8,
1129 946–949. <https://doi.org/10.1038/ngeo2557>
- 1130 Robles, M., 2022. Vegetation, climate, and human history of the Mediterranean basin: A Late-
1131 Glacial to Holocene reconstruction from Italy (Lake Matese) to Armenia (Lake Sevan)
1132 inferred from a multi-proxy approach (pollen, NPPs, brGDGTs, XRF) (PhD thesis).
1133 University of Molise, University of Montpellier, Campobasso, Montpellier.
- 1134 Robles, M., Peyron, O., Brugiapaglia, E., Ménot, G., Dugerdil, L., Ollivier, V., Ansanay-Alex,
1135 S., Develle, A.-L., Tozalakyan, P., Meliksetian, K., Sahakyan, K., Sahakyan, L., Perello,
1136 B., Badalyan, R., Colombié, C., Joannin, S., 2022. Impact of climate changes on
1137 vegetation and human societies during the Holocene in the South Caucasus (Vanevan,
1138 Armenia): A multiproxy approach including pollen, NPPs and brGDGTs. *Quaternary*
1139 *Science Reviews* 277, 107297. <https://doi.org/10.1016/j.quascirev.2021.107297>
- 1140 Rodrigo-Gámiz, M., García-Alix, A., Jiménez-Moreno, G., Ramos-Román, M.J., Camuera, J.,
1141 Toney, J.L., Sachse, D., Anderson, R.S., Sinninghe Damsté, J.S., 2022. Paleoclimate
1142 reconstruction of the last 36 kyr based on branched glycerol dialkyl glycerol tetraethers
1143 in the Padul palaeolake record (Sierra Nevada, southern Iberian Peninsula). *Quaternary*
1144 *Science Reviews* 281, 107434. <https://doi.org/10.1016/j.quascirev.2022.107434>
- 1145 Russell, J.M., Hopmans, E.C., Loomis, S.E., Liang, J., Sinninghe Damsté, J.S., 2018.
1146 Distributions of 5- and 6-methyl branched glycerol dialkyl glycerol tetraethers



- 1147 (brGDGTs) in East African lake sediment: Effects of temperature, pH, and new
1148 lacustrine paleotemperature calibrations. *Organic Geochemistry* 117, 56–69.
1149 <https://doi.org/10.1016/j.orggeochem.2017.12.003>
- 1150 Sadori, L., 2018. The Lateglacial and Holocene vegetation and climate history of Lago di
1151 Mezzano (central Italy). *Quaternary Science Reviews* 202, 30–44.
1152 <https://doi.org/10.1016/j.quascirev.2018.09.004>
- 1153 Salonen, J.S., Korpela, M., Williams, J.W., Luoto, M., 2019. Machine-learning based
1154 reconstructions of primary and secondary climate variables from North American and
1155 European fossil pollen data. *Sci Rep* 9, 15805. <https://doi.org/10.1038/s41598-019-52293-4>
- 1156
- 1157 Samartin, S., Heiri, O., Joos, F., Renssen, H., Franke, J., Brönnimann, S., Tinner, W., 2017.
1158 Warm Mediterranean mid-Holocene summers inferred from fossil midge assemblages.
1159 *Nature Geosci* 10, 207–212. <https://doi.org/10.1038/ngeo2891>
- 1160 Sanchi, L., Ménot, G., Bard, E., 2014. Insights into continental temperatures in the northwestern
1161 Black Sea area during the Last Glacial period using branched tetraether lipids.
1162 *Quaternary Science Reviews* 84, 98–108.
1163 <https://doi.org/10.1016/j.quascirev.2013.11.013>
- 1164 Sbaiffi, L., Wezel, F.C., Curzi, G., Zoppi, U., 2004. Millennial- to centennial-scale
1165 palaeoclimatic variations during Termination I and the Holocene in the central
1166 Mediterranean Sea. *Global and Planetary Change* 40, 201–217.
1167 [https://doi.org/10.1016/S0921-8181\(03\)00111-5](https://doi.org/10.1016/S0921-8181(03)00111-5)
- 1168 Sicre, M.-A., Siani, G., Genty, D., Kallel, N., Essallami, L., 2013. Seemingly divergent sea
1169 surface temperature proxy records in the central Mediterranean during the last deglacial.
1170 *Climate of the Past* 9, 1375–1383. <https://doi.org/10.5194/cpd-9-683-2013>
- 1171 Sinninghe Damsté, J.S., Rijpstra, W.I.C., Foessel, B.U., Huber, K.J., Overmann, J., Nakagawa,
1172 S., Kim, J.J., Dunfield, P.F., Dedysh, S.N., Villanueva, L., 2018. An overview of the
1173 occurrence of ether- and ester-linked iso-diabolic acid membrane lipids in microbial
1174 cultures of the Acidobacteria: Implications for brGDGT paleoproxies for temperature
1175 and pH. *Organic Geochemistry* 124, 63–76.
1176 <https://doi.org/10.1016/j.orggeochem.2018.07.006>
- 1177 Smith, V.C., Isaia, R., Pearce, N.J.G., 2011. Tephrostratigraphy and glass compositions of post-
1178 15 kyr Campi Flegrei eruptions: implications for eruption history and
1179 chronostratigraphic markers. *Quaternary Science Reviews* 30, 3638–3660.
1180 <https://doi.org/10.1016/j.quascirev.2011.07.012>
- 1181 Stockhecke, M., Bechtel, A., Peterse, F., Guillemot, T., Schubert, C.J., 2021. Temperature,
1182 precipitation, and vegetation changes in the Eastern Mediterranean over the last
1183 deglaciation and Dansgaard-Oeschger events. *Palaeogeography, Palaeoclimatology,
1184 Palaeoecology* 577, 110535. <https://doi.org/10.1016/j.palaeo.2021.110535>
- 1185 Sun, Q., Chu, G., Liu, M., Xie, M., Li, S., Ling, Y., Wang, X., Shi, L., Jia, G., Lü, H., 2011.
1186 Distributions and temperature dependence of branched glycerol dialkyl glycerol
1187 tetraethers in recent lacustrine sediments from China and Nepal. *J. Geophys. Res.* 116,
1188 G01008. <https://doi.org/10.1029/2010JG001365>
- 1189 Taffetani, F., Catorci, A., Ciaschetti, G., Cutini, M., Di Martino, L., Frattaroli, A.R., Paura, B.,
1190 Pirone, G., Rismondo, M., Zitti, S., 2012. The *Quercus cerris* woods of the alliance
1191 *Carpinion orientalis* Horvat 1958 in Italy. *Plant Biosystems - An International Journal
1192 Dealing with all Aspects of Plant Biology* 146, 918–953.
1193 <https://doi.org/10.1080/11263504.2012.682613>
- 1194 Tarroso, P., Carrión, J., Dorado-Valiño, M., Queiroz, P., Santos, L., Valdeolmillos-Rodríguez,
1195 A., Célio Alves, P., Brito, J.C., Cheddadi, R., 2016. Spatial climate dynamics in the



- 1196 Iberian Peninsula since 15 000 yr BP. *Climate of the Past* 12, 1137–1149.
1197 <https://doi.org/10.5194/cp-12-1137-2016>
- 1198 ter Braak, C.J.F., Juggins, S., 1993. Weighted averaging partial least squares regression (WA-
1199 PLS): an improved method for reconstructing environmental variables from species
1200 assemblages 18.
- 1201 ter Braak, C.J.F., van Dam, H., 1989. Inferring pH from diatoms: a comparison of old and new
1202 calibration methods. *Hydrobiologia* 178, 209–223.
1203 <https://doi.org/10.1007/BF00006028>
- 1204 Tomlinson, E.L., Arienzo, I., Civetta, L., Wulf, S., Smith, V.C., Hardiman, M., Lane, C.S.,
1205 Carandente, A., Orsi, G., Rosi, M., Müller, W., Menzies, M.A., 2012. Geochemistry of
1206 the Phlegraean Fields (Italy) proximal sources for major Mediterranean tephra:
1207 Implications for the dispersal of Plinian and co-ignimbritic components of explosive
1208 eruptions. *Geochimica et Cosmochimica Acta* 93, 102–128.
1209 <https://doi.org/10.1016/j.gca.2012.05.043>
- 1210 Valente, E., Buscher, J.T., Jourdan, F., Petrosino, P., Reddy, S.M., Tavani, S., Corradetti, A.,
1211 Ascione, A., 2019. Constraining mountain front tectonic activity in extensional setting
1212 from geomorphology and Quaternary stratigraphy: A case study from the Matese ridge,
1213 southern Apennines. *Quaternary Science Reviews* 219, 47–67.
1214 <https://doi.org/10.1016/j.quascirev.2019.07.001>
- 1215 Van Geel, B., 2002. Non-Pollen Palynomorphs, in: Smol, J.P., Birks, H.J.B., Last, W.M.,
1216 Bradley, R.S., Alverson, K. (Eds.), *Tracking Environmental Change Using Lake*
1217 *Sediments, Developments in Paleoenvironmental Research*. Springer Netherlands,
1218 Dordrecht, pp. 99–119. https://doi.org/10.1007/0-306-47668-1_6
- 1219 Vescovi, E., Kaltenrieder, P., Tinner, W., 2010. Late-Glacial and Holocene vegetation history
1220 of Pavullo nel Frignano (Northern Apennines, Italy). *Review of Palaeobotany and*
1221 *Palynology* 160, 32–45. <https://doi.org/10.1016/j.revpalbo.2010.01.002>
- 1222 Walker, M., Lowe, J., Blockley, S.P.E., Bryant, C., Coombes, P., Davies, S., Hardiman, M.,
1223 Turney, C.S.M., Watson, J., 2012. Lateglacial and early Holocene palaeoenvironmental
1224 ‘events’ in Sluggan Bog, Northern Ireland: comparisons with the Greenland NGRIP
1225 GICC05 event stratigraphy. *Quaternary Science Reviews* 36, 124–138.
1226 <https://doi.org/10.1016/j.quascirev.2011.09.008>
- 1227 Watson, B.I., Williams, J.W., Russell, J.M., Jackson, S.T., Shane, L., Lowell, T.V., 2018.
1228 Temperature variations in the southern Great Lakes during the last deglaciation:
1229 Comparison between pollen and GDGT proxies. *Quaternary Science Reviews* 182, 78–
1230 92. <https://doi.org/10.1016/j.quascirev.2017.12.011>
- 1231 Weijers, J.W.H., Panoto, E., van Bleijswijk, J., Schouten, S., Rijpstra, W.I.C., Balk, M., Stams,
1232 A.J.M., Damsté, J.S.S., 2009. Constraints on the Biological Source(s) of the Orphan
1233 Branched Tetraether Membrane Lipids. *Geomicrobiology Journal* 26, 402–414.
1234 <https://doi.org/10.1080/01490450902937293>
- 1235 Weijers, J.W.H., Schouten, S., Spaargaren, O.C., Sinninghe Damsté, J.S., 2006. Occurrence
1236 and distribution of tetraether membrane lipids in soils: Implications for the use of the
1237 TEX86 proxy and the BIT index. *Organic Geochemistry* 37, 1680–1693.
1238 <https://doi.org/10.1016/j.orggeochem.2006.07.018>
- 1239 Weijers, J.W.H., Schouten, S., van den Donker, J.C., Hopmans, E.C., Sinninghe Damsté, J.S.,
1240 2007. Environmental controls on bacterial tetraether membrane lipid distribution in
1241 soils. *Geochimica et Cosmochimica Acta* 71, 703–713.
1242 <https://doi.org/10.1016/j.gca.2006.10.003>
- 1243 Wulf, S., Kraml, M., Brauer, A., Keller, J., Negendank, J.F.W., 2004. Tephrochronology of the
1244 100ka lacustrine sediment record of Lago Grande di Monticchio (southern Italy).
1245 *Quaternary International* 122, 7–30. <https://doi.org/10.1016/j.quaint.2004.01.028>



- 1246 Wulf, S., Kraml, M., Keller, J., 2008. Towards a detailed distal tephrostratigraphy in the Central
1247 Mediterranean: The last 20,000 yrs record of Lago Grande di Monticchio. *Journal of*
1248 *Volcanology and Geothermal Research* 177, 118–132.
1249 <https://doi.org/10.1016/j.jvolgeores.2007.10.009>
1250 Yang, H., Pancost, R.D., Dang, X., Zhou, X., Evershed, R.P., Xiao, G., Tang, C., Gao, L., Guo,
1251 Z., Xie, S., 2014. Correlations between microbial tetraether lipids and environmental
1252 variables in Chinese soils: Optimizing the paleo-reconstructions in semi-arid and arid
1253 regions. *Geochimica et Cosmochimica Acta* 126, 49–69.
1254 <https://doi.org/10.1016/j.gca.2013.10.041>
1255
1256